Stress, pore pressure, and dynamically constrained hydrocarbon columns in the South Eugene Island 330 field, northern Gulf of Mexico

Thomas Finkbeiner, Mark Zoback, Peter Flemings, and Beth Stump

ABSTRACT

Hydrocarbon phase pressures at the peak of two severely overpressured reservoirs in the South Eugene Island 330 field, Gulf of Mexico, converge on the minimum principal stress of the top seal. We interpret that the system is dynamically constrained by the stress field present through either fault slip or hydraulic fracturing. In two fault blocks of a shallower, moderately overpressured reservoir sand, hydrocarbon phase pressures are within a range of critical pore pressure values for slip to occur on the bounding growth faults. We interpret that pore pressures in this system are also dynamically controlled. We introduce a dynamic capacity model to describe a critical reservoir pore pressure value that corresponds to either the sealing capacity of the fault against which the sand abuts or the pressure required to hydraulically fracture the overlying shale or fault. This critical pore pressure is a function of the state of stress in the overlying shale and the pore pressure in the sand. We require that the reservoir pore pressure at the top of the structure be greater than in the overlying shale. The four remaining reservoirs studied in the field exhibit reservoir pressures well below critical values for dynamic failure and are, therefore, considered static. All reservoirs that are dynamically constrained are characterized by short oil columns, whereas the reservoirs having static conditions have very long gas and oil columns.

INTRODUCTION

Several young and rapidly formed sedimentary basins exist around the world in which significant amounts of petroleum have migrated considerable vertical distances (i.e., several kilometers) through

Manuscript received December 15, 1998; revised manuscript received June 28, 2000; final acceptance August 31, 2000.

AUTHORS

THOMAS FINKBEINER ~ *GeoMechanics International, 250 Cambridge Avenue, Suite 103, Palo Alto, California, 94306; thomas@geomi.com*

Thomas Finkbeiner started his career in geophysics at the University of Karlsruhe, Germany. In 1992, he enrolled in the Department of Physics at Stanford University from where he received his M.S. degree in exploration and development in 1994 and his Ph.D. in 1998. Since the fall of 1998 Thomas has been working for GeoMechanics International as a specialist in reservoir geomechanics and a consultant for the petroleum industry in wellbore stability and in-situ stress.

MARK ZOBACK ~ *Department of Geophysics, Stanford University, Mitchell Building, Stanford, California, 94305; zoback@pangea.stanford.edu*

Mark Zoback received a B.S. degree in geophysics from the University of Arizona and his M.S. degree and Ph.D. in geophysics from Stanford University. He is a professor in the Department of Geophysics at Stanford. His previous experience includes working as a geophysicist with Amoco Production Co. and at the U.S. Geological Survey. He is also senior scientific advisor with GeoMechanics International in Palo Alto, California.

PETER FLEMINGS ~ *Geosciences Department, Pennsylvania State University, 442 Deike, University Park, Pennsylvania, 16802; flemings@geosc.psu.edu*

Peter B. Flemings is an associate professor with the Pennsylvania State University Department of Geosciences. He received his B.A. degree from Dartmouth College, and both an M.S. degree and Ph.D. in geology from Cornell University. Before joining Penn State, he was an associate research scientist at Lamont-Doherty Earth Observatory of Columbia University and the Crosby Distinguished Lecturer at the Massachusetts Institute of Technology. His research focuses on the study of fluid flow in sedimentary basins.

Beth Stump ~ *Texaco Worldwide Exploration & Production, 400 Poydras Street, New Orleans, Louisiana, 70160; stumpbb@texaco.com*

Beth Bishop Stump received both B.S. (1993) and M.S. (1998) degrees from Pennsylvania State University. Currently, she is working as a development geoscientist with Texaco Exploration & Production. She is a member of AAPG and the New Orleans Geological Society.

ACKNOWLEDGEMENTS

This research was financed by the Gas Research Institute under contract no. 5095-260-3558 and the Stanford Rock and Borehole Geophysics (SRB) consortium. Richard Parker of the Gas Research Institute provided valuable support for this project. Martin Traugott of Amoco helped us with many useful comments and suggestions. We would like to thank Pennzoil, Shell, and Texaco for generously providing the data used in this analysis. We appreciate the careful review of this manuscript by Jim Handschy and John Leftwich.

thick sequences of low-permeability shale (e.g., Nigeria, Gulf of Mexico, southeast Asia, Trinidad) (Holland et al., 1990; Nehring, 1991; Grauls and Baleix, 1994; Heppard et al., 1998). In this paper, we introduce a conceptual model, which we call the dynamic capacity model, to formalize two dynamic mechanisms (hydraulic fracturing and flow along active shear fractures) by which petroleum migration in these sedimentary basins may occur by enhanced fracture permeability. For both of these dynamic mechanisms, precise knowledge of in-situ state of stress and pore pressures conditions is required.

Faults have long been known to act as conduits for fluid flow (see review by Hickman et al. [1995]). Hooper (1991) raised the possibility that in many petroleum reservoirs faults may seal or conduct fluids at different times (or space) along the same fault plane. In the past, it was argued that the sealing or nonsealing capacity of a fault is dependent only upon the capillary properties of the fault gauge zone or the top seal (e.g., Smith, 1966), and leakage (i.e., fluid migration) is largely dominated by Darcian flow within the matrix. If, however, permeabilities are very low and capillary entry pressures become extremely high (e.g., as in shales), different mechanisms must provide enhanced permeability for fluids to migrate efficiently. Watts (1987) argued that in this scenario seal failure may occur by hydraulic fracturing. More recently, numerous publications have given the issue of fracture permeability controlling hydrocarbon entrapment and migration more importance. Leach (1993a–c) argues that hydrocarbons in south Louisiana Tertiary sediments have migrated vertically along faults by means of periodic hydraulic fracturing. Gaarenstroom et al. (1993) recognized more explicitly that faults control pressure distribution and compartmentalization in the central North Sea. Similarly, Grauls and Baleix (1994) attributed efficient transfer of liquid hydrocarbons in a sedimentary basin in southeast Asia to the presence of faults and fractures. These authors specifically argue that effective stress is an important factor for fluid flow and indicate that knowledge of the in-situ state of stress is vital for a fundamental understanding of distribution and prediction of pore pressures in sedimentary basins. Common to all these authors is the presumption that natural hydraulic fracturing is the dominant mechanism for providing the necessary fracture permeability. For this mechanism to operate, pore pressures are required to be as high as the least principal stress in the overlying strata (Rubey and Hubbert, 1959; Nur and Walder, 1990).

Alternatively, fracture permeability can also be enhanced by shear failure along active faults. Sibson (1992) proposed episodic fluid flow along rupturing faults associated with vein deposits in a "fault-valve" fashion. Barton et al. (1995) presented strong evidence from wells drilled in crystalline rock to argue that faults that are optimally oriented for shear failure (i.e., critically stressed) have increased permeability and conduct fluids. Noncritically stressed faults, in contrast, appear to not provide fluid migration pathways. Ingram and Urai (1997) argued in a general

sense that these mechanisms may also be operative in sedimentary basins, and more specifically, Engelder and Leftwich (1997) proposed such mechanisms for fluid migration in the oil and gas fields of south Texas.

In support of the dynamic capacity model introduced in this paper, we further investigated both dynamic mechanisms (hydraulic fracturing and failure along shear fractures) to determine whether reservoir pore pressures, hydrocarbon columns, and fluid flow can be controlled by fracture permeability in a state of dynamic equilibrium with the ambient state of stress. To evaluate whether either mechanism is operative, knowledge of the in-situ state of stress and pore pressure conditions is needed for both shale units and sand reservoirs. We outlined the required in-situ pore pressure and stress conditions for each mechanism and carefully tested the model in eight sand reservoirs and overlying shales of the South Eugene Island (SEI) 330 field, Gulf of Mexico. In fact, the data suggest that pore pressures and hydrocarbon column heights in moderately and severely overpressured reservoirs of the SEI 330 field appear to be limited by the present-day stress field.

DYNAMICALLY CONSTRAINED HYDROCARBONS

Areas undergoing rapid sedimentation like the Gulf of Mexico are commonly characterized by a normal faulting environment where the overburden is the maximum principal stress (i.e., $S_{hmin} \leq S_{Hmax} \leq S_v$). In such areas the pore pressures in compacting shales are generally expected to be higher than in adjacent sands units because of the shale's low permeability and relatively poor drainage during compaction. Models have been published, however, that predict the contrary (i.e., pore pressures in sands are higher than in adjacent shales) under appropriate circumstances. The centroid model is one such; at the top of a tilting, fluid-filled sand layer, higher pore pressures develop relative to the immediately adjacent, impermeable shales. This phenomenon is achieved by structural relief that induces differential sediment loading. The centroid model was first introduced by Dickinson (1953) and was further elaborated on by England et al. (1987) and Traugott and Heppard (1994), who coined its name. Stump et al. (1998) described and quantified this model and applied it to the sedimentary sequences of the SEI 330 field.

The dynamic capacity model is a modified version of the centroid model. We consider not only relative values of pore pressures in sands and adjacent shale units but also the ambient state of stress in the shales that might control dynamic mechanisms for fluid migration and accumulation. Two important aspects of the dynamic capacity model contrast it with the centroid model. First, we consider the pore pressure as measured in the reservoir (P_p^{ss}) regardless of whether it is the water or a hydrocarbon phase. Hence, P_p^{ss} at the top of the structure accounts not only for the pressure difference between sand and shale as a result of structural relief but also for the hydrocarbon buoyancy effect, as prescribed by the centroid model. As a result, the pressure difference between sand and shale is even greater. Second, we consider dynamic mechanisms for fluid flow. These mechanisms allow us to establish bounds for the maximum column heights supported by the system because it is the sealing capacity of the overlying top seal or the fault against which the reservoir abuts that controls critical pore pressure in the underlying sand.

Figure 1 summarizes three possible hydrocarbon migration scenarios by establishing relationships between pore pressure in the reservoir sand and in-situ state of stress in the adjacent shale. Two of these scenarios (Figure 1A, B) relate to the dynamic capacity model through dynamic migration mechanisms (i.e., they involve sudden failure of the top seal controlled by specific pore pressure and stress conditions). The third scenario (Figure 1C), in contrast, presents a static migration mechanism. The Mohr circles in Figure 1 define the required relative stress and pore pressure magnitudes for the dynamic migration mechanisms to be invoked by the sand-shale system. These pore pressures and stresses are defined precisely at the point in the top seal where the sand is juxtaposed against shale and possibly a bounding fault. Notice that we plotted these Mohr diagrams using total stresses rather than effective stresses as commonly done. Although the effective stress concept (e.g., Terzaghi, 1943) fundamentally underlies our model, the representation of the Mohr diagrams in total stress space has the advantage of directly comparing the required relationships between the critical pore pressure and actual pore pressures and stresses in both shales and sands. Furthermore, we implicitly assume that the top seal has zero cohesive strength. We consider this to be a reasonable assumption because the sediments in the SEI 300 field are poorly consolidated (Ostermeier, 1993; Chang and Zoback, 1998).

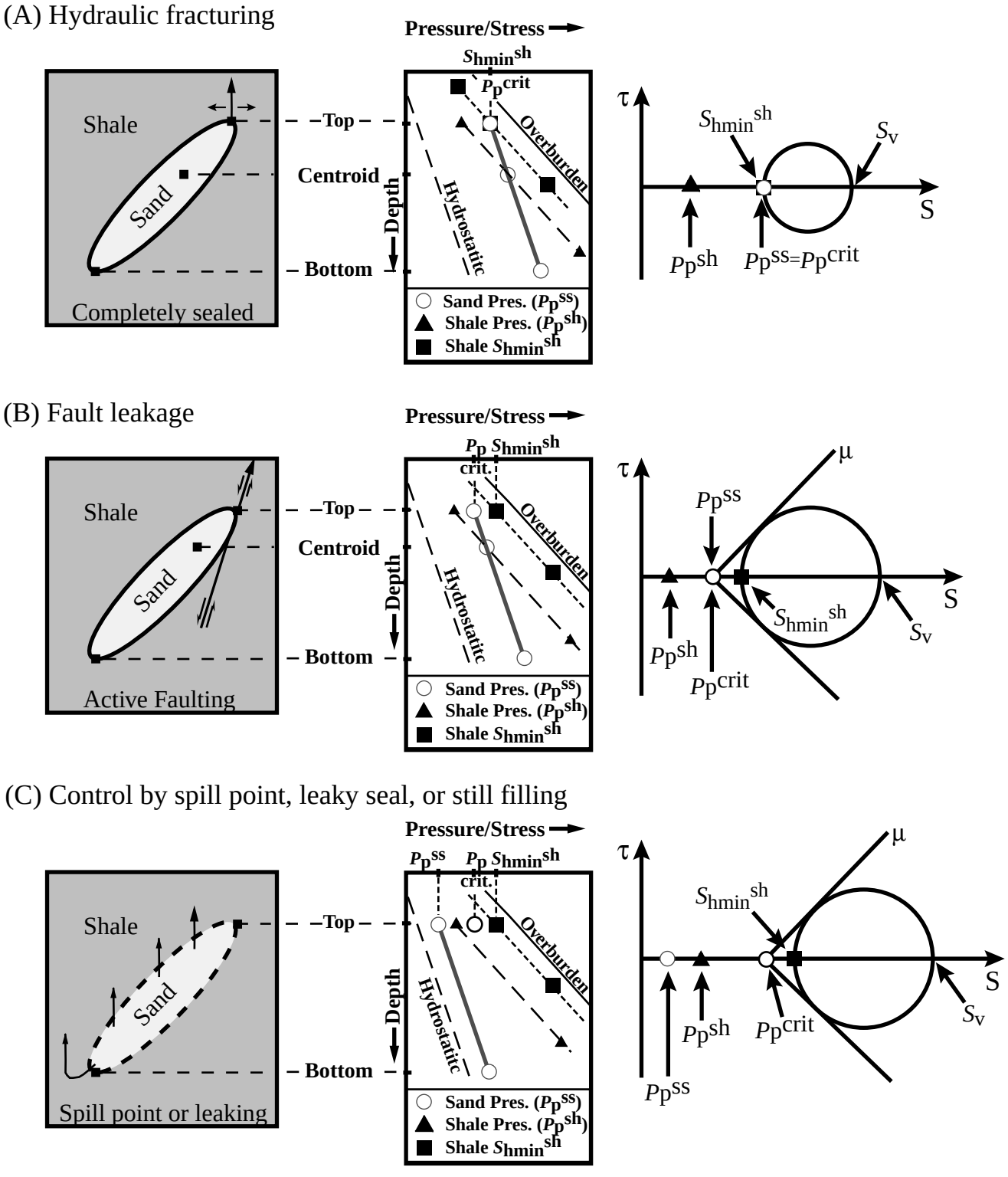

Figure 1A, B exhibits a state of dynamic equilibrium in which the pore pressure in the sand (P_p^{ss}) has reached a maximum possible value. We call this maximum pressure value the dynamic capacity of the reservoir (P_p^{crit}). Beyond this critical pore pressure, failure occurs, allowing fluids to escape. In Figure 1A this mechanism is hydraulic fracturing (e.g., Hubbert and Willis, 1957; Nur and Walder, 1990), where the least

Figure 1. The dynamic capacity model. Left: tilting sand lens that is filled with fluids and surrounded by shales. Middle: pore pressures and stresses as a function of depth for this reservoir system. Shale pressures (P_p^{sh}, black triangle) follow the lithostatic gradient (i.e., overburden) recording undrained conditions. Sand pressures (P_p^{ss}) record internal hydraulic communication and have the pressure gradient of the fluid phase. The centroid is the depth at which the shale pore pressure (P_p^{sh}) equals the sand pore pressure (P_p^{ss}) (Traugott and Heppard, 1994). Right: Mohr diagrams illustrate relative pore pressures and stress conditions at the top of the sand lens (i.e., the sand-shale interface). Total stresses are plotted, and S_v denotes the overburden stress. **(A)** Migration by hydraulic fracturing. $P_p^{ss} > P_p^{sh}$ and P_p^{ss} equals the least principal stress in the shale (S_{hmin}^{sh}). **(B)** Migration by fault leakage. $P_p^{ss} > P_p^{sh}$ and P_p^{ss} equals the critical pore pressure (P_p^{crit}) for which the reservoir bounding fault starts to slip (indicated by the Coulomb friction line touching the Mohr circle for a coefficient of friction of μ). Notice, in contrast to case (A), P_p^{crit} is lower than S_{hmin}^{sh}; yet, P_p^{ss} is at dynamic capacity. **(C)** Migration controlled by a spill point or leaky seal. $P_p^{ss} < P_p^{crit}$ (i.e., not in dynamic equilibrium), and P_p^{ss} can be either above or below P_p^{sh}.

principal effective stress (σ_{hmin}^{sh}) is zero. In other words, P_p^{ss} has to be equal to the least principal total stress in the shale (S_{hmin}^{sh}) for the top seal to be breached (i.e., $\sigma_{hmin}^{sh} = S_{hmin}^{sh} - P_p^{ss} = 0$).

The second dynamic fluid flow mechanism is by frictional failure along optimally oriented, preexisting faults when the shear stress resolved along the fault plane overcomes its frictional resistance and the fault slips (Figure 1B). For this mechanism, the critical pore pressure in the sand is not required to be as high as the least principal total stress in the overlying shale ($P_p^{crit} < S_{hmin}^{sh}$). In other words, the least principal effective stress in the shale has a finite, positive value and is a function of the frictional properties (μ) of the slipping fault. This concept is based on Coulomb frictional faulting theory (e.g., Jaeger and Cook, 1979) according to $\sigma_{hmin}^{sh} / \sigma_v = [(\mu^2 + 1)^{1/2} + \mu]^{-2} = f(\mu)$, where σ_{hmin}^{sh}, σ_v, and μ are the least principal effective stress in the shale, the overburden effective stress, and the coefficient of sliding friction, respectively. Shear failure has been associated with dilatancy (pore-volume increase caused by the formation of microcracks), resultant permeability increase, and fluid expulsion along fault zones (e.g., Makurat, 1985; Antonellini and Aydin, 1994). Also, geometric irregularities along the fault plane tend to cause areas of opening at the time the fault slips. Notice that a necessary condition for either of these two dynamic mechanisms (hydraulic fracturing or fault slip) to be operative is for the pore pressure in the sand to be higher relative to the overlying shales (i.e., $P_p^{ss} > P_p^{sh}$), because it is the pressure in the underlying sands that has to induce failure in the overlying shale for fluid flow to occur.

The third scenario (Figure 1C) indicates pore pressures in both sand and shale that are considerably lower than the critical value P_p^{crit}, and we consider these reservoirs not to be filled to their dynamic capacity. The sand pore pressure can be greater or less than the pore pressure of the bounding shale, because the reservoir is in a relatively static state not involving any dynamic failure mechanisms. In this case the sand could still be filling, it could be leaking (e.g., because of insufficient seal capacity of the top seal), or the column height could be spill-point controlled. Table 1 summarizes the dynamic capacity model by showing the required relative magnitudes between pore pressures and stresses for the three mechanisms just discussed.

In Figure 2 we illustrate the dynamic capacity model in the light of a sand reservoir that is filling over time with oil or gas until the hydrocarbon column has reached a specific height. The maximum column the reservoir sand can support depends on (1) the initial water-phase pressure in the reservoir, (2) the mechanisms by which fluids migrate (as described in Figure 1), and (3) the density of the hydrocarbon phase. Figure 2A, B shows developing hydrocarbon column

Table 1. Required Relative Pore Pressure Magnitudes for Both Sand and Shale for the Three Fluid Migration Mechanisms of the Dynamic Capacity Model*

Migration Mechanism	Type	Shale Pore Pressure (P_p^{sh})	Sand Pore Pressure (P_p^{ss})	Critical Pore Pressure (P_p^{crit})
Hydraulic fracturing	Dynamic	$< P_p^{ss}$ and $< P_p^{crit}$	$= P_p^{crit}$	$= S_{hmin}^{sh}$
Fault leakage/slip	Dynamic	$< P_p^{ss}$ and $< P_p^{crit}$	$= P_p^{crit}$	$< S_{hmin}^{sh}$ and $f(\mu)$
Spill point, leaky seal, or still filling	Static	($< P_p^{ss}$ or $> P_p^{ss}$) and $< P_p^{crit}$	$< P_p^{crit}$	n/a

*P_p^{ss} = sand pore pressure; P_p^{sh} = shale pore pressure; P_p^{crit} = critical pore pressure; S_{hmin}^{sh} = least principal total stress in the shale; n/a = not available.

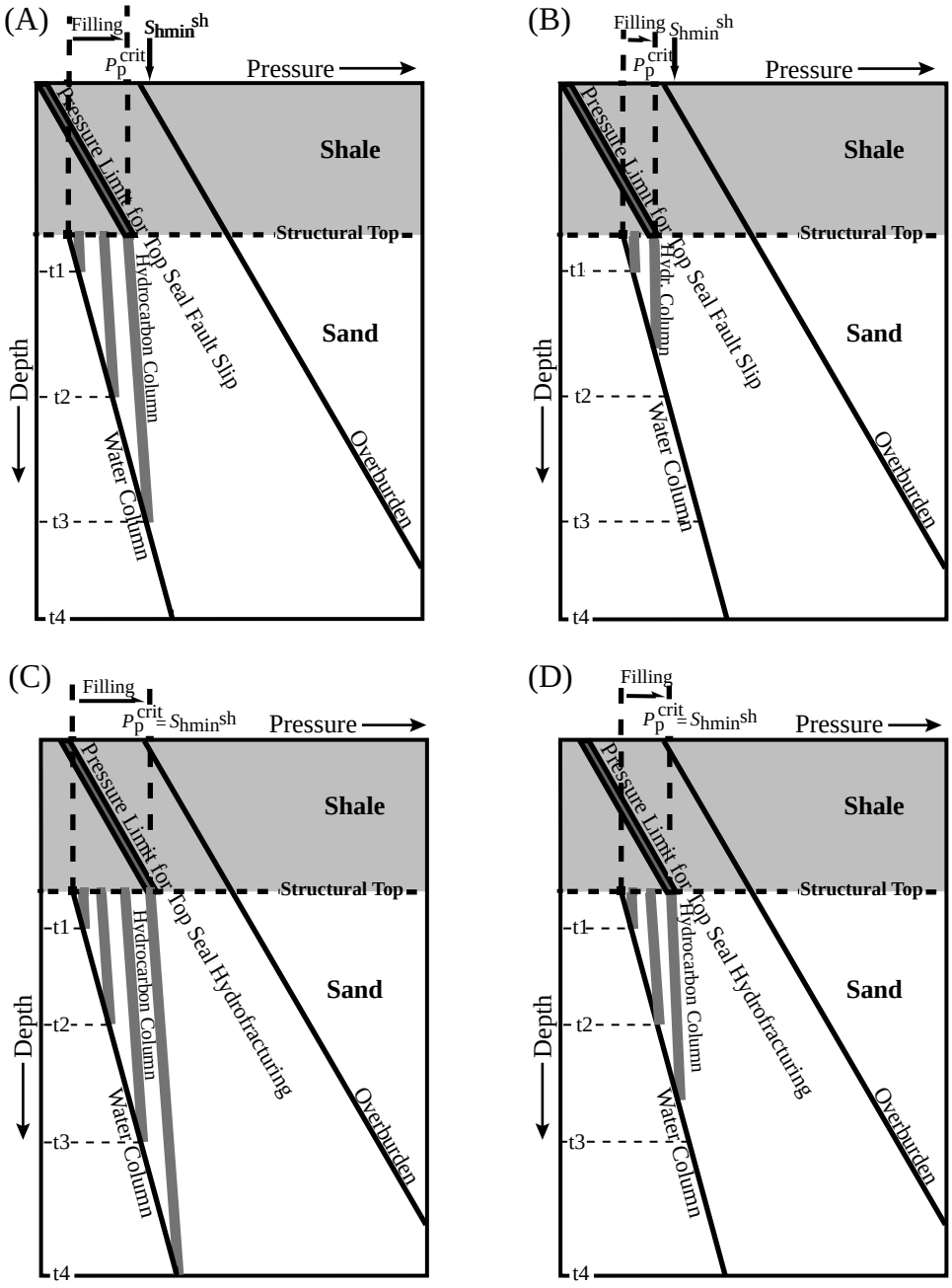

Figure 2. Conceptual model of filling a sand reservoir with hydrocarbons (gray columns) as a function of initial water pressure (black) and time (outlined with four time steps t_1 through t_4). The critical pore pressure or pressure limit (i.e., P_p^{crit}; wide gray line) is the maximum capacity of the reservoir beyond which dynamic fluid flow mechanisms are invoked. Fluid flow along active faults during slip events is shown in (A) and (B). Hydraulic fracturing, where $P_p^{ss} = S_{hmin}^{sh}$, is exhibited in (B) and (C). Initially low reservoir water-phase pore pressures allow development of larger hydrocarbon columns over time before dynamic capacity (P_p^{crit}) is reached (cases A and C). Initially high reservoir water-phase pore pressures allow only small hydrocarbon columns to accumulate, and dynamic equilibrium (P_p^{crit}) is reached at an earlier time (cases B and D). Notice how hydraulic fracturing allows larger columns to develop over longer time relative to active fault slip for the same initial water-phase pressure: compare (A) with (C) and (B) with (D).

heights controlled by fault slip, and Figure 2C, D exhibits columns controlled by hydraulic fracturing. When the reservoir sands have low initial water-phase pore pressures, large hydrocarbon columns can accumulate over time before the dynamic capacity (i.e., P_p^{crit}) is reached (Figure 2A, C). When the reservoir sands have high initial water-phase pore pressures, the dynamic reservoir capacity is reached at much earlier times, and relatively smaller hydrocarbon columns develop (Figure 2B, D). Because P_p^{crit} has to be equal to S_{hmin}^{sh} for hydraulic fracturing to occur, the resulting hydrocarbon columns are larger (Figure 2A, B) as opposed to the situation for fluid flow along active faults, for which smaller columns accumulate because $P_p^{crit} < S_{hmin}^{sh}$ (Figure 2C, D). Conversely, if the reservoir has not reached its dynamic capacity because the observed hydrocarbon column is small and not in dynamic equilibrium, we can conclude that the reservoir is still filling, has a spill point, or is leaking (i.e., is under statically controlled fluid flow).

Thus, we believe hydrocarbon column heights are potentially controlled by the state of stress at the reservoir-fault contact in a manner that when the pore pressure at the top of the sand (P_p^{ss}) reaches the value

required for the fault to fail in the shale (P_p^{crit}), either by slip (Figure 1B) or by hydraulic fracturing (Figure 1A), an episode of fluid flow occurs. In this scenario, the reservoir has reached its maximum hydrocarbon column and is at dynamic capacity. In other words, the hydrocarbon column in the reservoir is in dynamic equilibrium with the state of stress in the overlying shale top seal.

THE SOUTH EUGENE ISLAND 330 FIELD

Overview and Data

We applied the dynamic capacity concept outlined in the previous section to the SEI 330 field. This field is located about 160 km offshore Louisiana in the Gulf of Mexico (Holland et al., 1990) (Figure 3A). Recoverable reserves have been estimated at 307 million bbl of liquid hydrocarbons and 1.65 tcf of gas (Holland et al., 1990), which are distributed in more than 25 different sand layers segmented by shales and normal faults into at least 100 structurally or stratigraphically distinct reservoirs (Figure 3B). The hydrocarbons sourced from older sediments are believed to have migrated vertically over significant distances (Holland et al., 1990).

This giant oil and gas field is in a Pliocene–Pleistocene salt-withdrawal minibasin bounded to the north and east by a regional (down to the south) growth fault system and to the south by an antithetic fault system (Alexander and Flemings, 1995). Beneath the OI sands the stratigraphy is largely shale dominated, and from the OI sands upward it is more sand dominated. Pressures are closely tied to this stratigraphic architecture. In the shale-prone region, beneath the OI sands, severe overpressuring occurs. Because the pressures follow these stratigraphic surfaces, and because there is significant offset across the growth fault at this depth, overpressures are much deeper in the hanging wall than in the footwall (Gordon and Flemings, 1998).

Structure maps based on three-dimensional seismic and wire-line data (provided by Pennzoil, the operator of Blocks 330 and 316) enabled us to analyze eight reservoirs from three different sands in five separate fault blocks. The three different sands are the Lentic (footwall, fault blocks A and C), the OI-1 (minibasin, fault blocks A, B, C, and E), and the JD (minibasin, fault blocks A and B) (Figure 3A, B) (see Alexander and Flemings [1995] and Holland et al. [1990] for detailed discussion). We determined the depths of the structural highs in each of the eight reservoirs from the structure maps and associated column heights using additional information on fluid contact levels (i.e., oil-water and gas-oil contacts). The data extracted from these maps are summarized in Table 2. We estimate these values to be accurate to ± 5 m for the structural highs and contact levels. This uncertainty translates to a ± 10 m uncertainty for the column heights. The reservoir tops of the stratigraphically highest sand (JD) shale out, whereas the structurally highest points of the deeper sand reservoirs (OI-1 and Lentic) abut against growth faults.

To determine in-situ pressure and stress, we used a database consisting of downhole measurements from nearly 30 wells (provided by Pennzoil, Texaco, and Shell). These measurements include repeated pressure surveys (including in-situ temperature and oil gravity values), sonic logs, and leak-off tests (LOTs) and formation integrity tests (FITs) (Finkbeiner et al., 1997, unpublished results). We used the earliest pressure records in the reservoir sands to get the pore pressure conditions prior to production while the reservoir was still in an undepleted state (Table 3). We estimated the pressure surveys (such as repeat formation tests [RFTs]) to be accurate to approximately ± 0.07 MPa (± 10 psi). Given pore pressures at some level within the reservoir sand, we calculated fluid densities and extrapolated the reservoir pressures to the structural tops. Some reservoirs have both oil and gas columns. In this case, we calculated the pressure using the oil gradient in the oil column between oil-water and gas-oil contacts and the gas gradient above the gas-oil contact to the top of the sand. We followed the approach of Batzle and Wang (1992) to obtain the live oil density (i.e., with the maximum gas dissolved) based on the in-situ reservoir temperature and API number of the oil. Oil gradients range from 5.66 MPa/km (0.25 psi/ft) to 7.69 MPa/km (0.34 psi/ft) (Table 3) and are accurate to within 5%. We assumed a constant gradient of 2.26 MPa/km (0.1 psi/ft) for the gas gradient, which is a reasonable assumption as verified from calculation of gas densities along structures using pressure, volume, temperature (PVT) data. The resulting fluid column heights and pressures were then simply obtained by calculating the depth intervals from the fluid contacts (e.g., water-oil or oil-gas) to the top of the structure and using the respective fluid gradients (Table 3).

The minimum principal stress in the top seal (S_{hmin}^{sh}) was determined based on LOT and FIT

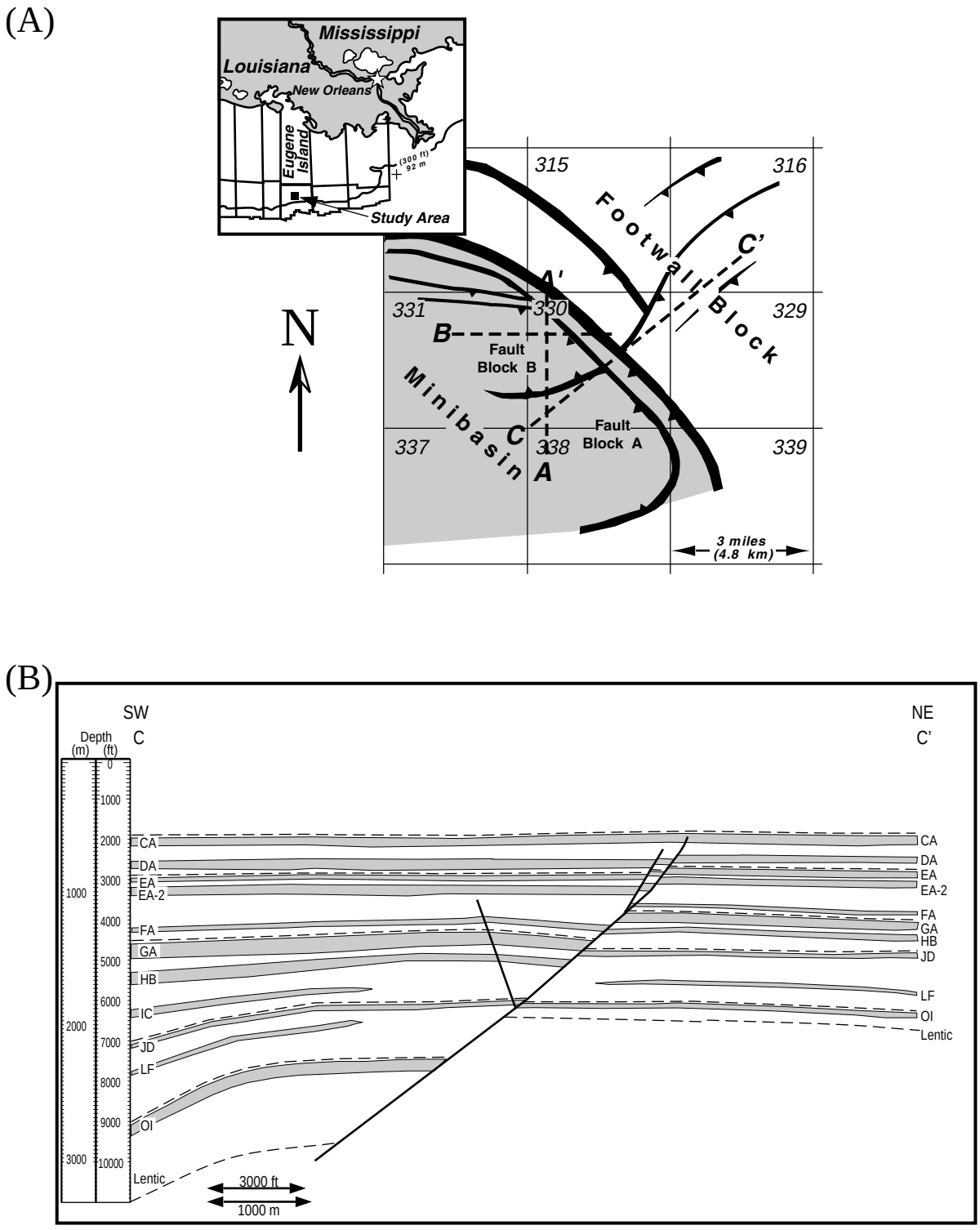

Figure 3. **(A)** Base map of the SEI 330 field outlining the minibasin and the footwall separated by the basin bounding growth fault system. The dashed line CC′ marks the transect of the cross section in (B). Cross sections along transects AA′ and BB′ are shown in Figures 10 and 11, respectively. **(B)** Cross section through the SEI 330 field along transect CC′ shown in (A). Reservoir sands are displayed in gray, labeled accordingly with their names; dashed lines are the corresponding flooding surfaces (modified from D. S. Gordon and P. B. Flemings, 1998, personal communication).

Table 2. Fluid Contact Levels and Column Heights in the SEI 330 Reservoirs Studied*

Reservoir Sand	Fault Block	Top of structure, SSTVD (m)	Oil-water contact, SSTVD (m)	Gas-oil contact, SSTVD (m)	Oil column (m)	Gas column (m)
Lentic	Footwall, FB-A	2228.7 (±5)	2302.1 (±5)	n/a	53.4 (±10)	n/a
	Footwall, FB-C	1936.0 (±5)	2132.0 (±5)	n/a	196.0 (±10)	n/a
OI-1	A	2109.8 (±5)	2275.6 (±5)	n/a	165.9 (±10)	n/a
	B	2048.8 (±5)	2689.3 (±5)	2655.5 (±5)	33.8 (±10)	606.7 (±10)
	C	2240.9 (±5)	2689.3 (±5)	2628.7 (±5)	60.7 (±10)	387.8 (±10)
	E	2042.7 (±5)	2195.1 (±5)	n/a	152.4 (±10)	n/a
JD	A	1768.3 (±5)	2079.3 (±5)	2039.9 (±5)	39.3 (±10)	271.6 (±10)
	B	1768.3 (±5)	2067.4 (±5)	2061.0 (±5)	6.4 (±10)	292.7 (±10)

*This information was extracted from structural maps shown in Figures 4, 7, 9. n/a = not available.

Table 3. Initial Sand Pore Pressures and Corresponding Live Oil Densities in the SEI 330 Reservoirs Studied*

Reservoir Sand	Fault Block	Well	SSTVD (m)	P_p^{ss} (MPa)	S_v (MPa)	$\lambda_{ss} = P_p^{ss}/S_v$	Live Oil Gradient (MPa/km)
Lentic	Footwall, FB-A	316/A-3ST	2257.0	42.79 (±0.07)	47.54 (±0.3)	0.90 (±0.07)	7.69 (±0.38)
	Footwall, FB-C	316/A-4	2113.1	39.07 (±0.07)	43.90 (±0.3)	0.89 (±0.08)	6.79 (±0.34)
		316/A-8	2029.0	39.20 (±0.07)	42.15 (±0.3)	0.93 (±0.08)	6.79 (±0.34)
OI-1	A	330/B-3	2266.5	39.23 (±0.07)	47.27 (±0.3)	0.83 (±0.07)	6.56 (±0.33)
	B	330/B-14	2147.3	36.43 (±0.07)	44.98 (±0.3)	0.81 (±0.07)	5.66 (±0.28)
	C	330/A-3	2294.8	36.64 (±0.07)	47.58 (±0.3)	0.77 (±0.06)	7.24 (±0.36)
	E	330/A-23	2100.6	36.99 (±0.07)	44.57 (±0.3)	0.83 (±0.07)	7.24 (±0.36)
JD	A	330/B-13	1871.3	25.68 (±0.07)	38.91 (±0.3)	0.66 (±0.07)	7.24 (±0.36)
	B	330/B-17	2014.0	25.21 (±0.07)	41.33 (±0.3)	0.61 (±0.06)	7.24 (±0.36)

*Pore pressure is normalized by the overburden ($\lambda_{ss} = P_p^{ss}/S_v$). The trajectories for the wells from which data were acquired are displayed in Figures 4, 7, and 9. Pore pressures are from pressure surveys. We calculated live oil gradient following the approach by Batzle and Wang (1992). The overburden was calculated by integrating the density log from well 331/#1 (provided by Pennzoil and Texaco).

measurements (Table 4). In contrast to LOTs, FITs do not hydraulically fracture the formation; hence, they generally present a lower bound for the minimum principal stress. Similar to the procedure with the shale pore pressure data, we used linear regressions to extrapolate S_{hmin}^{sh} to the structural highs.

Shale pressures (P_p^{sh}) were calculated from a porosity-effective stress method based on sonic log data (Hart et al., 1995; Stump et al., 1998). Prediction of shale pore pressures from wire-line logs using this equivalent depth method has been attempted in the industry for many years. Results are generally associated with a considerable amount of uncertainty because this method predicts shale pore pressures only reasonably well if the rock's compaction history has exclusively followed a loading trend. In the event of late-stage pore pressure increase, however, (caused, for example, by fluid recharge, hydrocarbon generation, thermal expansion, or clay dehydration), the reservoir would experience effective unloading. This effect would result in an underprediction of pore pressure because permanent rock deformation accompanying the initial compaction during loading inhibits porosity recovery during pressurization. These unloading effects limit the applicability of the porosity-effective stress methods for pore pressure predictions. In the case of field SEI 330, we assume that these unloading effects have not affected the shale. Mello and Karner (1996) and Burrus (1998) pointed out that the oil maturation and illitization windows are located deeper in the strata because of rapid sedimentation and sediment undercompaction, which resulted in a depressed thermal gradient. Thus, potential fluid generation and unloading in response to hydrocarbon maturation or clay

Table 4. Least Principal Total Stresses (S_{hmin}^{sh}) in the Shales Adjacent to the SEI 330 Reservoirs Studied*

Fault Block	Well	SSTVD (m)	Type	Closest Sand	S_{hmin}^{sh} (MPa)	S_v (MPa)	S_{hmin}^{sh}/S_v
A	330/B-2	2370.7	FIT	OI-1	46.59 (±0.31)	49.56 (±0.3)	0.94 (±0.01)
	330/B-7	2337.5	LOT	OI-1	46.78 (±0.59)	49.24 (±0.3)	0.95 (±0.02)
	330/C-10	2047.9	LOT	OI-1	40.32 (±0.31)	42.89 (±0.3)	0.94 (±0.01)
	330/C-12	1992.4	LOT	MG-3	39.24 (±0.42)	41.74 (±0.3)	0.94 (±0.02)
	330/C-16	2096.6	FIT	OI-1	40.01 (±1.03)	43.97 (±0.3)	0.91 (±0.03)
B	330/A-11	2312.5	FIT	OI-1	45.46 (±1.26)	48.36 (±0.3)	0.94 (±0.03)
	330/A-5	2063.7	FIT	LF	39.64 (±1.31)	43.09 (±0.3)	0.92 (±0.04)
	330/C-8	2182.6	LOT	OI-1	44.23 (±0.53)	45.60 (±0.3)	0.97 (±0.02)
C	n/a	n/a	n/a	n/a	n/a	n/a	n/a
E	330/A-6ST	1981.7	LOT	OI-1	39.03 (±0.66)	41.52 (±0.3)	0.94 (±0.02)
Footwall	316/A-12	1953.7	FIT	Lentic	39.91 (±0.39)	40.72 (±0.3)	0.98 (±0.02)
	330/#9	2020.4	LOT		42.59 (±0.96)	42.17 (±0.3)	1.01 (±0.03)
	330/A-20ST	2175.0	Hydrofrac		44.79 (±0.07)	45.24 (±0.3)	0.99 (±0.01)

*Leak-off tests (LOTs) and formation integrity tests (FITs) were provided by Pennzoil and Texaco. We used structural maps provided by Pennzoil to identify the closest sand. The trajectories for the wells from which data were acquired are displayed in Figures 4, 7, and 9. The overburden was calculated by integrating the density log from well 331/#1 (provided by Pennzoil and Texaco).

dehydration are not issues for the SEI 330 area. Further, Burrus (1998) claimed that compaction models for overpressured sediments in the Gulf of Mexico do not account for poroelastic effects, which can greatly affect in-situ stress and pore pressure. Although we agree that poroelastic effects can significantly alter the state of stress in reservoirs during pore pressure reduction caused by production (e.g., Engelder and Fischer, 1994; Segall et al., 1994; Segall and Fitzgerald, 1996;), it is not necessary to address this issue for either the shales or the undepleted SEI 330 reservoirs. Therefore, we assume that shale porosity should predict in-situ shale pressure with reasonable accuracy. Note that the dynamic capacity concept we introduce in this paper does not require an accurate determination of shale pore pressure. Instead, the pore pressure in the sand at the top of the reservoir structure simply has to be higher than the pore pressure in the overlying top seal. Thus, the porosity-effective stress method we use is adequate for determination of the relative relationship between reservoir and adjacent shale pore pressures.

Hence, for sonic logs that penetrated the reservoir bounding shales, we calculated pore pressure values at the closest point to the eight reservoirs. We believe that the pressure errors introduced through the various parameters required for the porosity-effective stress model are within 1 MPa (150 psi). This small error range results from the fact that the values of the model parameters and their associated uncertainties were all derived specifically for the South Eugene Island field through analysis of a substantial number of logs, and these showed only minor variations throughout the field. In other words, the parameter values are tailored to predict shale pore pressures specifically in SEI 330, and caution should be used in transferring them to other areas because considerable variations are quite feasible, which can affect the predictions considerably. In Table 5 we list the well names and depths for which we derived the original sonic data, the parameter values required for the calculations, and the resulting shale pore pressures using the model discussed in the previous section. For a detailed formulation and discussion of the model, refer to work by Hart et al. (1995) and Stump et al. (1998). In each fault block we then fit a linear regression to the predicted shale pore pressures to estimate the pressure in the top seal adjacent to the structural highs of the reservoir sands.

The overburden stress (S_v) was calculated using an average gradient derived from integration of the density logs. This method accounts for the undercompacted and highly overpressured nature of the SEI sediments. The overburden gradients for all wells range between 20.5 MPa/km (0.91 psi/ft) and 21.2 MPa/km (0.94 psi/ft), which is significantly lower than the commonly assumed constant gradient of 22.6 MPa/km (1 psi/ft). The calculations are associated with an uncertainty of approximately 0.3 MPa/km (0.015 psi/ft), or 1.7%, based on determination of the overburden in several wells.

Table 5. Well Names and Parameter Values from Which Shale Pore Pressures Were Calculated*

Well	Fault Block	SSTVD (m)	Δt (μs/m)	Δt_{ma} (μs/m)	φ	φ_0	β (MPa^{-1})	S_v (MPa)	P_p^{sh} (MPa)
316/A-1	Footwall	2000.6	432.22	204	0.290	0.386	0.03683	41.44	33.66 ($\pm$1)
316/A-6	Footwall	2132.9	426.80	204	0.286	0.386	0.03683	44.29	36.12 ($\pm$1)
316/A-12	Footwall	2034.5	450.30	204	0.303	0.386	0.03683	42.10	35.50 ($\pm$1)
330/B-13	A	2263.7	388.32	204	0.251	0.386	0.03683	47.44	35.79 ($\pm$1)
331/#1	B	2530.8	357.37	204	0.225	0.386	0.03132	53.46	36.28 ($\pm$1)
331/A-4	B	2644.2	368.60	204	0.236	0.386	0.03132	55.90	40.23 ($\pm$1)
330/A-20ST	E	2032.3	388.01	204	0.254	0.386	0.03683	42.14	30.78 ($\pm$1)
330/B-13	A	1844.5	365.07	204	0.233	0.386	0.03683	38.43	24.71 ($\pm$1)
338/#5	A	2042.4	387.36	204	0.253	0.386	0.03132	42.53	29.09 ($\pm$1)
330/A-20ST2	D	1947.9	342.99	204	0.211	0.386	0.03683	40.31	23.88 ($\pm$1)
330/A-22	B	1969.5	348.17	204	0.216	0.386	0.03683	40.78	25.03 ($\pm$1)
331/#1	B	1951.5	379.57	204	0.246	0.386	0.03132	40.39	26.07 ($\pm$1)

*Refer to Hart et al. (1995) and Stump et al. (1998) for the porosity-effective stress model we applied. The parameter definitions are listed in the nomenclature table (see Appendix).

In Table 6 we list all pore pressure and stress values required to apply the dynamic capacity model at the top seals of the eight SEI 330 reservoirs.

Characterization of Pore Pressure and Stress Conditions

The three sands investigated in this study (Lentic, OI-1, and JD sands) (Figure 3B) cap three depositional cycles in the SEI 330 field and exhibit characteristic pore pressure and stress conditions. For each reservoir from these three stratigraphic layers we carefully examined pore pressures at their structural tops, in-situ stress of the overlying shale caps, and hydrocarbon column heights. This information is summarized in Tables 3–6. Subsequently, we analyzed our results in view of the dynamic capacity model just presented.

First, we calculated the critical pore pressure value (P_p^{crit}) based on Coulomb frictional failure theory:

$$P_p^{crit} = [S_{hmin}^{sh} - f(\mu) \times S_v]/[1 - f(\mu)] \quad (1)$$

where $f(\mu) = [(\mu^2 + 1)^{1/2} + \mu]^{-2}$, and μ is the coefficient of sliding friction. We calculate an upper and lower bound for P_p^{crit} using two different values for μ that seem reasonable for the SEI 330 field: $\mu = 0.3$ (lower bound) and $\mu = 0.6$ (upper bound) (Table 7). The lower bound results from laboratory experiments with clay under undrained conditions (e.g., Wang et al., 1979, 1980). The upper bound, in contrast, is a typical value found in field measurements in many areas around the world (e.g., see reviews in Zoback and Healy [1984, 1992]; Brudy et al. [1997]).

Second, we compared the pore pressure at the top of each reservoir sand to the range of P_p^{crit} values and drew some implications about fluid flow and the observed hydrocarbon column heights in each of the eight reservoirs. To evaluate how close the hydrocarbon column is to dynamic failure in a reservoir, we introduced a new parameter, the dynamic capacity stress ratio (C_{dyn}):

$$C_{dyn} = [S_{hmin}^{sh} - P_p^{ss}]/[S_v - P_p^{ss}] \quad (2)$$

C_{dyn} resembles the effective stress ratio $K = [S_{hmin}^{sh} - P_p^{sh}]/[S_v - P_p^{sh}]$ for shales. K has been given substantial attention in the literature (e.g., Pilkington, 1978; Traugott, 1997) because it describes the fracture gradient, an important parameter for drilling operations; however, there is one important difference between K and C_{dyn}: for the dynamic capacity concept, the driving parameter to invoke dynamic failure in the overlying shales is the critical pore pressure in the sand reservoir (P_p^{crit}). Therefore, with C_{dyn} we consider the reservoir pore pressure at the top of the structure (P_p^{ss}) and the least principal stress in the shale (S_{hmin}^{sh}). In the case of hydraulic fracturing (Figure 1A), $P_p^{crit} = S_{hmin}^{sh}$, and hence, $C_{dyn} = 0$. In the case of fluid flow along active faults (Figure 1B), $P_p^{crit} < S_{hmin}^{sh}$, and hence, $0 < C_{dyn} < 1$ depending upon the coefficient of friction, μ. Given $\mu = 0.3$ and $\mu = 0.6$ (upper and lower bound) we display the C_{dyn}

Table 6. Pore Pressures, Total Stresses, Dynamic Capacity Ratio (C_{dyn}),* and Shale Effective Stress Ratio** at the Top of the SEI 330 Reservoirs Studied†

Fault Block	Reservoir Sand	Top of Structure, SSTVD (m)	S_v (MPa)	P_p^{ss} (MPa)	λ_{ss}	S_{hmin}^{sh} (MPa)	S_{hmin}^{sh} Gradient (MPa/km)	C_{dyn}	P_p^{sh} (MPa)	P_p^{sh} Gradient (MPa/km)	λ_{sh}	K
A	JD	1768.3	36.75	24.99	0.68	34.04	21.26	0.77	24.14	21.49	0.66	0.78
	Ol-1	2109.8	44.33	38.21	0.86	41.32		0.51	31.54		0.71	0.76
B	JD	1768.3	36.43	24.66	0.68	33.43	23.07	0.74	22.22	16.97	0.61	0.79
	Ol-1	2048.8	42.53	35.90	0.84	39.93		0.61	26.98		0.63	0.83
C	Ol-1	2240.9	46.79	36.52	0.78	44.12	23.07	0.74	27.37	12.21	0.58	0.86
E	Ol-1	2042.7	42.41	36.57	0.86	39.90	23.07	0.57	31.01	28.05	0.73	0.78
Footwall	L-1, FB-A	2228.7	46.48	42.58	0.92	45.54	21.04	0.76	38.17	13.12	0.82	0.89
	L-1, FB-C	1936.0	40.32	38.60	0.96	39.42		0.47	33.11			0.87
				37.87	0.94			0.63				

*Calculated using equation 2.
**[$K = (S_{hmin}^{sh} - P_p^{sh})/(S_v - P_p^{sh})$]
†The tops of the structures are the same as in Table 2. We calculated the overburden by integrating density logs from nearby wells (provided by Pennzoil and Texaco). Sand pore pressures (P_p^{ss}) were derived using live oil densities following the approach by Batzle ad Wang (1992) and, where necessary, gas gradients of 2.62 MPa/km (0.1 psi/ft). We calculated total least principal stresses (S_{hmin}^{sh}) and pore pressure (P_p^{sh}) values and gradients in shales by linearly regressing the available values in each individual fault block.

values for each reservoir in Table 6. For comparison, Table 6 also lists the corresponding K values in the overlying shales. Table 7 shows the critical C_{dyn} values (C_{dyn}^{crit}) evaluated using P_p^{crit} for $\mu = 0.3$ and $\mu = 0.6$ for which the bounding faults would slip.

The Lentic Sand

The Lentic sand is the deepest reservoir sand in the SEI 330 field. It was deposited in an outer continental shelf to continental slope environment (Alexander and Flemings, 1995). Pore pressures prior to depletion are around 90% of the overburden. The data used for our study came from SEI 330 Block 316—the footwall side—of the minibasin bounding growth fault system (Figure 3A). The Lentic sand abuts two northeast-southwest–striking normal faults and subsidiary fault splays (Figure 4). A roughly east-west–striking antithetic normal fault subcompartmentalizes the sand into fault block A and fault block C. This antithetic normal fault does not entirely separate fault blocks A and C. Pennzoil geologists interpreted that complete closure and hydraulic decoupling between the two reservoirs is achieved by an apparent permeability barrier (shown as thick T dashes in Figure 4) further downdip to the east in fault block A (J. Austin, 2001, personal communication). The Lentic sand has 152.4 m (500 ft) to 274.4 m (900 ft) of structural relief within each fault block (Figure 4). The highest points of the reservoirs abut the normal faults near the southern lease boundary. In fault block A, we used the lowest known oil level as the reference level to calculate the oil column height. In both fault blocks, oil columns are less than 182.9 m (600 ft) (Table 2; Figure 5C, D).

Least principal stress magnitudes (S_{hmin}^{sh}) in the shales are derived from three different types of measurements conducted in the immediate vicinity of the Lentic sand (Table 4). The FIT and hydraulic fracture were carried out on the footwall side in Block 330 just to the southwest of the area shown in Figure 4. The LOT comes from the Pennzoil A-12, Block 316 well in fault block C (Figure 4). The hydraulic fracture test from the Pennzoil A-20ST, Block 330 well (Flemings et al., 1995) should accurately reflect the state of stress in the shale just above the Lentic sand. The state of stress in the shale on top of the Lentic sand obtained by a linear fit through the given data points suggests a near isotropic stress state (i.e., $S_{hmin}^{sh} \sim S_v$).

Pore pressures in the Lentic sand reach values greater than 90% of the overburden stress ($0.92 < \lambda_{ss} < 0.96$) (Tables 3, 6; Figure 5B). Water-phase pore

Table 7. Critical Reservoir Pore Pressures (P_p^{crit})* and Critical Effective Stress Ratios for Dynamic Capacity (C_{dyn}^{crit})** at the Top of the SEI 330 Reservoirs Studied for Two Coefficients of Friction (μ)†

Fault Block	Reservoir Sand	Top of Structure, SSTVD (m)	P_p^{crit} (MPa) ($\mu = 0.3$)	C_{dyn}^{crit} ($\mu = 0.3$)	P_p^{crit} (psi) ($\mu = 0.6$)	C_{dyn}^{crit} ($\mu = 0.6$)
A	JD	1768.3	30.7	0.55	32.8	0.32
	OI-1	2109.8	37.6	0.55	39.9	0.32
B	JD	1768.3	29.7	0.55	32.0	0.32
	OI-1	2048.8	36.7	0.55	38.7	0.32
C	OI-1	2240.9	40.8	0.55	42.9	0.32
E	OI-1	2042.7	36.8	0.55	38.7	0.32
Footwall	L-1, FB-A	2228.7	44.4	0.55	45.1	0.32
	L-1, FB-C	1936.0	38.3	0.55	39.0	0.32

*Calculated with equation 1.
**Calculated with equation 2 using P_p^{crit}.
†The tops of the structures are the same as in Table 2.

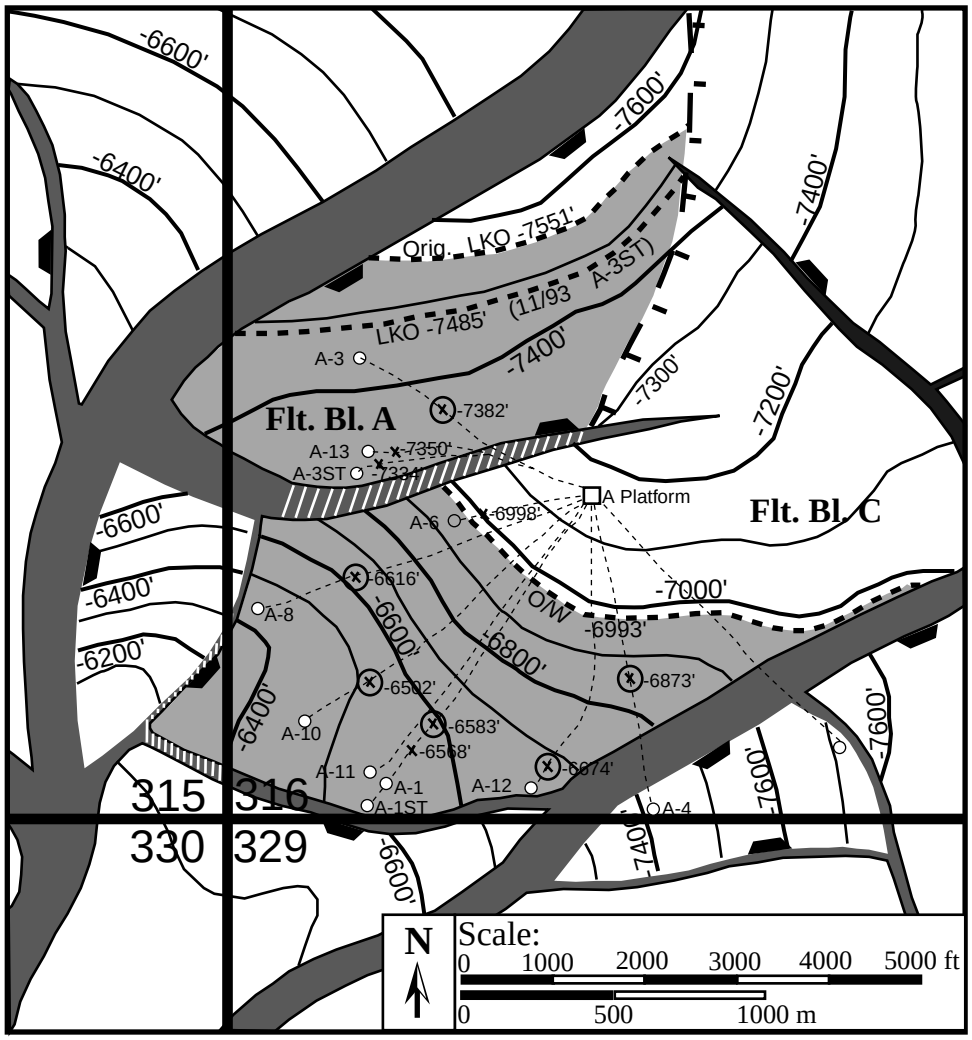

Figure 4. Structure map of the Lentic reservoir sand showing dominant structural features in the southwest corner of SEI 330 Block 316 and adjacent blocks. Depth contours are in feet SSTVD (conversion: 1 m = 3.28 ft). Well paths are displayed as thin dashed lines with points of reservoir penetration (crosses along well paths). Thick dashed lines display interpreted fluid contacts in the individual fault blocks (O/W = oil-water; LKO = lowest known oil). The associated depth intervals in the two reservoirs filled with oil are shown in gray. Thick T dashes in fault block A exhibit assumed permeability barriers. The hatched fault segments (white) indicate potential slip areas along which fluids could migrate (see text). This structure map was generated by Pennzoil based on three-dimensional seismic and log data. The normal faults are vertical projections of the fault plane onto the Lentic horizon; the downthrown side of the fault is marked by black ticks.

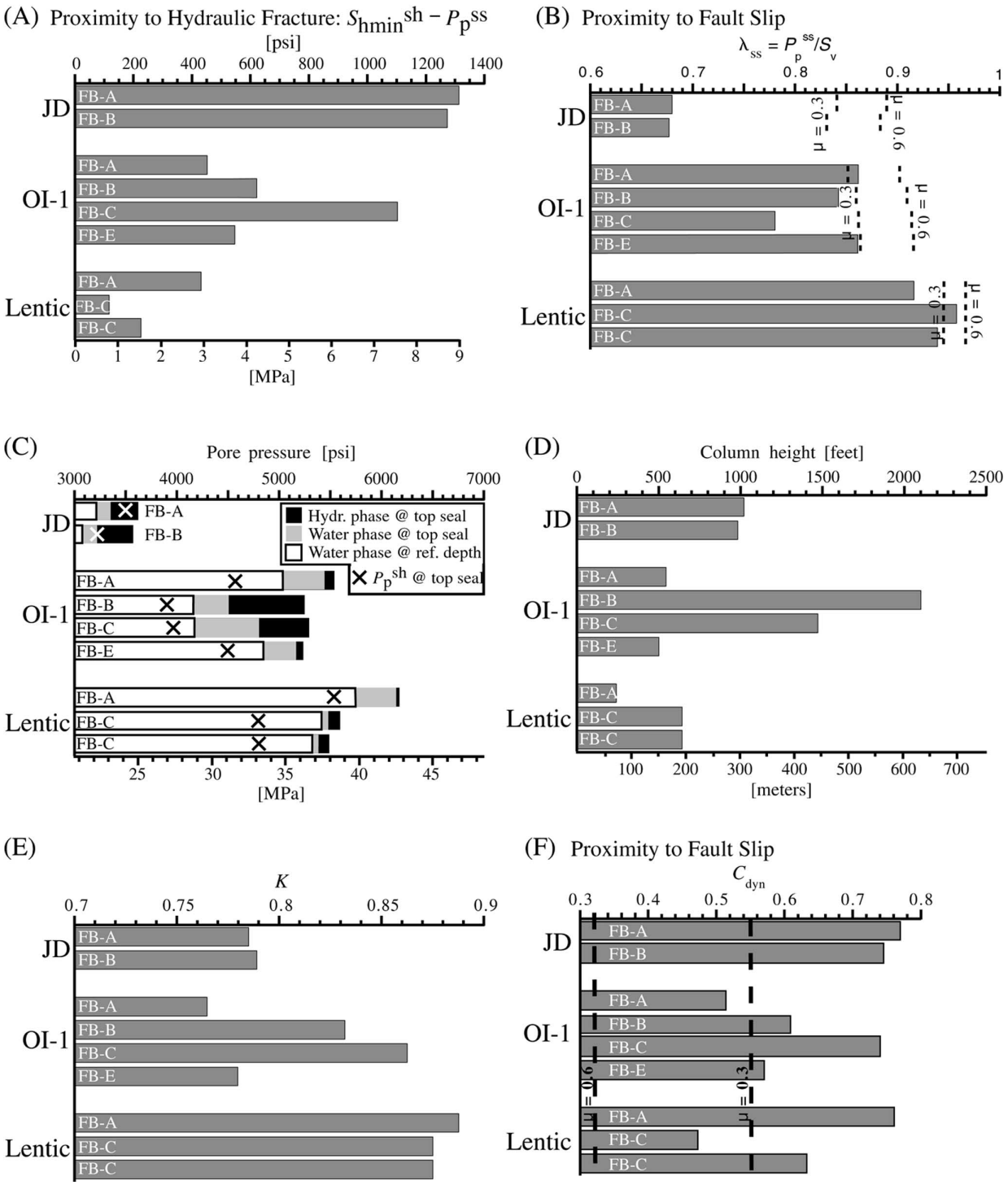

Figure 5. In-situ pore pressure and stress conditions at the top of the eight reservoirs in three SEI 330 sands. The abscissa displays the three sands in stratigraphic sequence. (A) Tendency for hydraulic fracturing indicated by the difference between least principal stress in the shale (S_{hmin}^{sh}) and reservoir pore pressure (P_p^{ss}). (B) Tendency for fault slip shown as normalized reservoir pore pressures (λ_{ss}). The dashed lines indicate lower and upper bound of critical pore pressures (P_p^{crit}) within the range of coefficients of friction (μ) between 0.3 and 0.6, respectively. (C) Hydrocarbon- (black column) and water- (gray column) phase pore pressure at top of the reservoirs (seal top). The difference between them indicates hydrocarbon column height. The white column displays the water-phase pore pressure at a specific reference datum (i.e., JD = 1677 m [5500 ft]; OI-1 = 1829 m [6000 ft]; Lentic = 1982 m [6500 ft] SSTVD). The cross shows the shale pressure (P_p^{sh}) at the top of the reservoirs. (D) Column heights for hydrocarbon phases. (E) Effective stress ratio (K) in the shale at the reservoir-seal interface. (F) Dynamic capacity stress ratio (C_{dyn}) as defined in equation 2 to display the tendency for fault slip. The two dashed lines indicate the two critical C_{dyn} values evaluated using P_p^{crit} for $\mu = 0.3$ and $\mu = 0.6$.

pressures at an equivalent depth do not match between fault blocks A and C, indicating compartmentalization (Figure 5C). In footwall block C, P_p^{ss} at the top of the structure is within approximately 0.69–1.38 MPa (100–200 psi) of the least principal stress in the shale (S_{hmin}^{sh}) (Figure 5A, B). The pore pressure at the top of the reservoir in footwall block A is also high and within 1.82 MPa (264 psi) of P_p^{crit} for $\mu = 0.3$ and within 2.97 MPa (430 psi) of S_{hmin}^{sh} (Figures 5B, 6).

Stump et al. (1998) derived shale pore pressures in three wells just above the Lentic sand. The shale is also highly overpressured; however, the magnitudes are less than in the sands (i.e., $\lambda_{sh} < \lambda_{ss}$) by about 9% (Table 6; Figure 5C). This fact fulfills the necessary requirement for the dynamic capacity mechanisms to operate because it is the pore pressure in the reservoir sand that drives the overlying sealing shale to failure.

As a result of the high overpressure in the shale, the near isotropic stress state, and low effective stresses, K is high (~0.9 [Table 6]), as is obvious from the shale stress gradient line in Figure 6, which is approximately 90% of the distance between the shale pressure and the overburden. This trend is typical for severely overpressured and undrained sediments of the Gulf Coast and has been reported in numerous publications (e.g., Althaus, 1977; Pilkington, 1978). Because overpressures at the top of the Lentic reservoirs are even more severe (i.e., P_p^{ss} is close to S_{hmin}^{sh}), we would expect C_{dyn} to approach zero or C_{dyn}^{crit} (Table 7) to indicate the proximity to dynamic failure; however, we find that C_{dyn} scatters between 0.46 and 0.76 (Table 6). Because the differential stress ($S_v - S_{hmin}^{sh}$) is so close to zero, the variations in P_p^{ss} cause the significant scatter in C_{dyn}. Therefore, the proximity of the oil columns to dynamic failure in this case is quite difficult to assess using C_{dyn}.

Figures 5A, B and 6 clearly show, however, that the pore pressures are close to both hydraulic fracturing and fault slip. In view of the dynamic capacity model, we find that the pore pressures in both fault blocks are not only near or within the lower and upper bound of P_p^{crit} but also approach the hydraulic fracture limit (Table 7), suggesting near dynamic failure conditions (i.e., slip along active faults as well as hydraulic fracturing) (Figures 5A, B; 6).

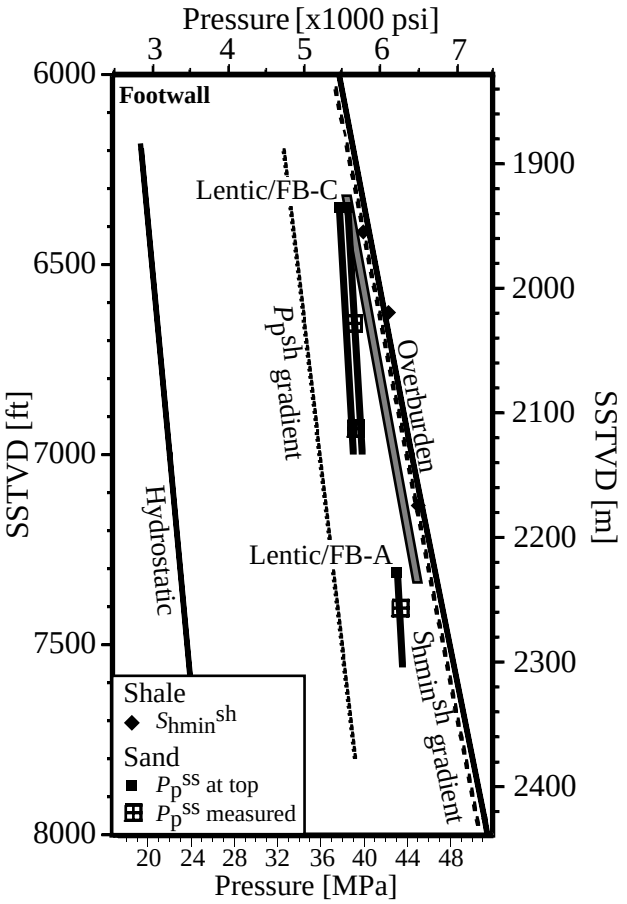

Figure 6. Pressure and stress state of the Lentic sand (located in Figure 4). Least principal stresses in shales (S_{hmin}^{sh}) are from leak-off tests (LOTs) and formation integrity tests (FITs). We also display the regression line for shale pore pressures (short dashes) and reservoir pore pressures (P_p^{ss}). The black squares represent the oil phase P_p^{ss} at the top of each sand (black for oil phase, gray for gas phase) calculated by using live oil gradients (Table 3). Solid lines represent hydrostatic and lithostatic gradients, and the dashed lines are linearly regressed gradients for P_p^{sh} and S_{hmin}^{sh}. The gray area paralleling the trends for least principal stress in the shale and the overburden indicates the range of critical pore pressures (for $0.3 < \mu < 0.6$; equation 1) for which the top seal reaches its frictional limit, the reservoir bounding fault slips, and the reservoir is at dynamic capacity.

The OI-1 Sand

The OI reservoirs are among the most productive in the SEI 330 field and were deposited near the shelf margin of the ancestral Mississippi delta system—a much shallower environment than the Lentic sand (Figure 3B) (Holland et al., 1990). The OI sequence comprises four individual sand cycles that are separated by transgressive shales (Alexander and Flemings, 1995). We focus our analysis on the reservoirs of the uppermost sand, the OI-1. The OI-1 is bounded by a concave-shaped, predominantly northwest-southeast–striking sequence of normal faults that constitute the main basin bounding growth fault system in the

SEI 330 field (Figure 7). On the downthrown side within the minibasin, several approximately east-west–striking normal faults subdivide the system into at least five different fault blocks that are sequentially labeled A through E. The offset along these normal faults is approximately 30.5 m (100 ft) (antithetic and subsidiary faults) to 243.9 m (800 ft) (main basin bounding growth fault) (Figure 7).

Fault blocks A, D, and E exhibit small oil columns (dark gray) of between 152.4 m (500 ft) and 167.7 m (550 ft). In contrast, the total column heights in B and C are quite large (640.2 and 457.3 m [2100 and 1500 ft], respectively) and characterized by long gas (light gray) and relatively short oil columns (Table 2; Figure 7). The OI-1 is moderately to severely overpressured, having λ_{ss} values that range from 0.77 to 0.83 (Table 3; Figures 5B, 8B).

Significant differences exist in the hydrocarbon-phase pressures and the water-phase pressures in the different OI-1 reservoirs. The hydrocarbon-phase pressure at the top of the structures in fault blocks B, C, and E are apparently equal, whereas the oil-phase

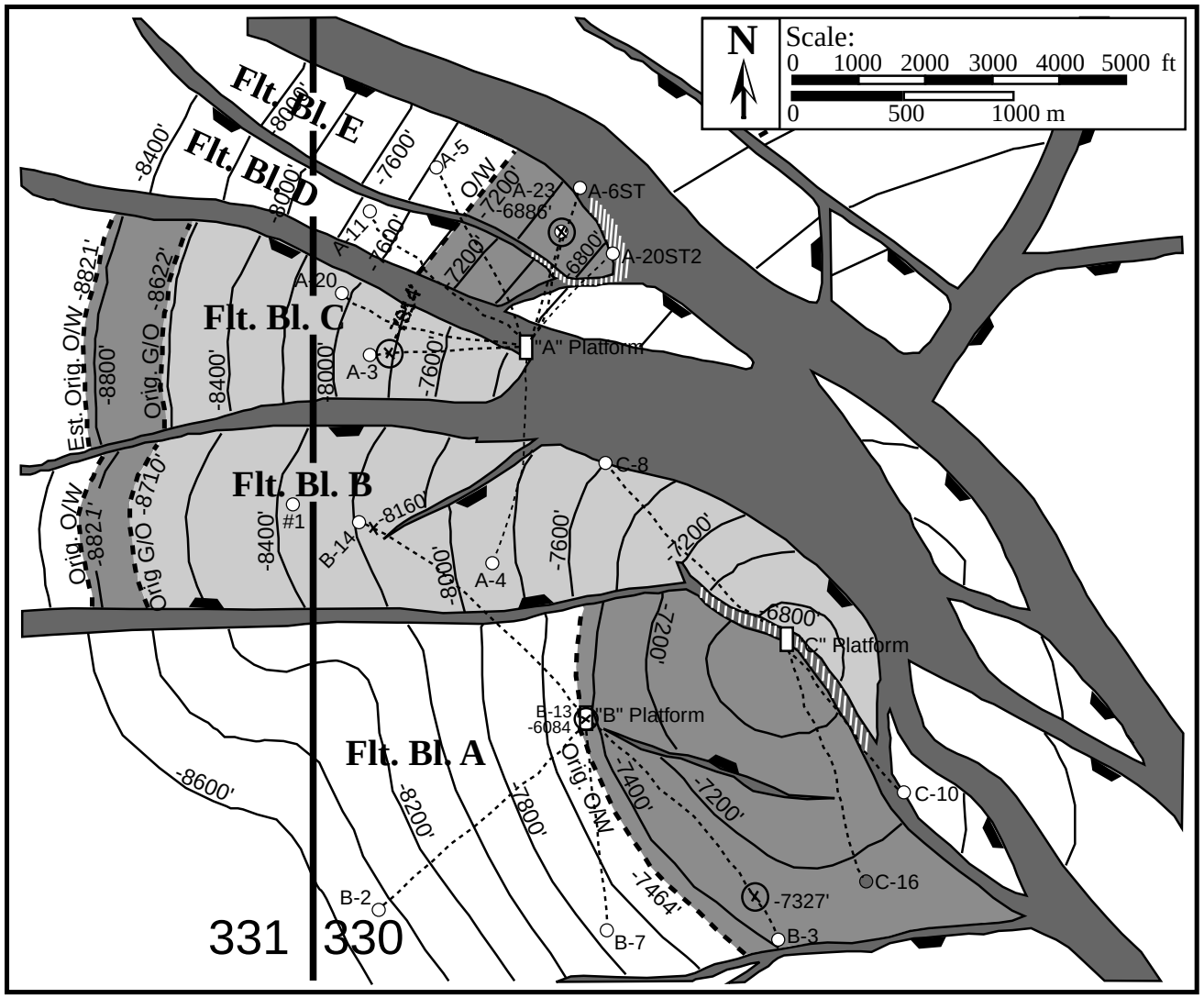

Figure 7. Structure map of the OI-1 reservoir sand for fault block 330 and parts of adjacent fault block 331. Depth contours are in feet SSTVD (conversion: 1 m = 3.28 ft). Well paths are shown as thin dashed lines with points of reservoir penetration (crosses along well paths). Thick dashed lines display interpreted fluid contacts and elevations in the individual fault blocks (O/W = oil-water; G/W = gas-water; LKO = lowest known oil). The depth intervals filled with oil and gas are shown in dark and light gray, respectively. The hatched fault segments (white) indicate potential slip areas along which fluids could migrate. Figure 4 caption describes how this map was generated.

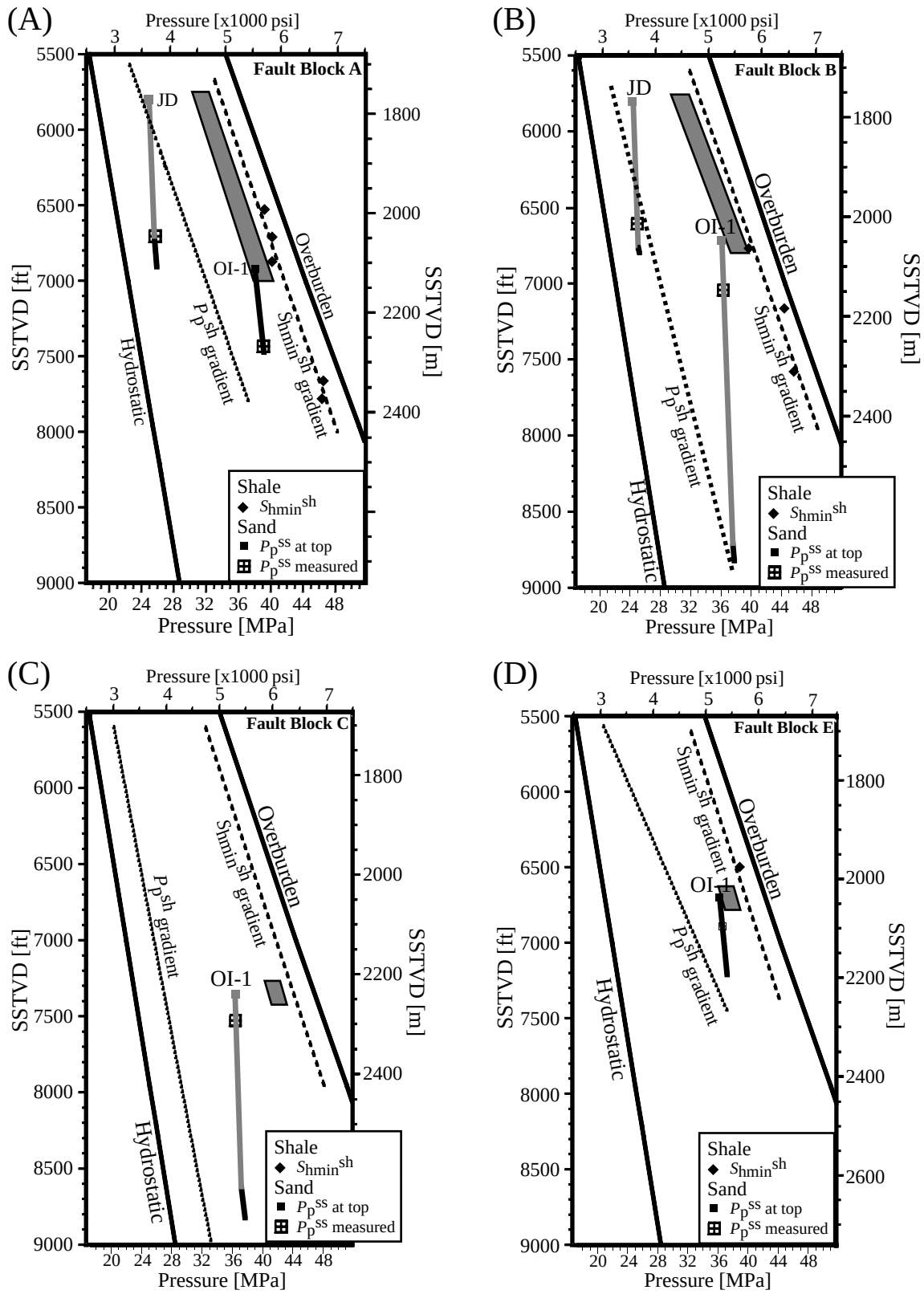

Figure 8. Pressure and stress state of the OI-1 (located in Figure 7) and JD (located in Figure 9) sands in minibasin fault blocks A **(A)**, B **(B)**, C **(C)**, and E **(D)**. Refer to Figure 6 caption for more details.

pressure at the top of fault block A is significantly higher (black bars in Figure 5C). This is true, although the column heights are much larger in fault blocks B and C and the structural tops in fault blocks B, C, and E are at different depths (Table 2). Furthermore, if we look at the water pressure at an equivalent depth, we see that there are sharp differences (white bars in Figure 5C). Pressures in fault blocks B and C are 3.45–4.83 MPa (500–700 psi) lower than in fault blocks A and E.

Predicted shale pore pressures (P_p^{sh}) as derived from the linear regressions exhibit moderate overpressures (λ_{sh} ranges from 0.69 to 0.76) (Table 6). In all cases, at the peak of the structure, the shale pressure is considerably less than the sand pressure (i.e., between l5 and 25%). Again, this fact is a necessary requirement for the dynamic capacity mechanisms to operate. Furthermore, shale pressures mirror the water-phase pressures recorded in the sand. At a given depth, shale pressures are lower in fault blocks B and C than in fault blocks A and E (Figure 5C).

The least principal stress in the shale (S_{hmin}^{sh}) lies at approximately 80% of the distance between the shale pressure (P_p^{sh}) and the overburden (S_v) (Figure 8A–D), which corresponds to a stress ratio (K) of around 0.8 (Figure 5E). This trend is well established in fault blocks A and B where multiple stress measurements were made in the vicinity of the OI-1 horizon. We inferred the S_{hmin}^{sh} trend in fault blocks C and E from adjacent fault block B because there is no or only one LOT available (Table 4).

In all fault blocks, hydrocarbon-phase pore pressures at the peak of the OI-1 structure are lower than the least principal stress in the shale (i.e., the difference between S_{hmin}^{sh} and P_p^{ss} is not zero) (Figure 5A). Consequently, the reservoirs are not at hydraulic fracturing conditions (Figure 1A); however, the OI-1 reservoir in fault blocks A and E are clearly within or at the window of critical pore pressures for frictional failure indicating dynamic equilibrium (Figures 5B; 8A, D). The reservoir pore pressure in fault blocks B and C, in contrast, are below the P_p^{crit} window (Figures 5B; 8B, C), suggesting they are not dynamically controlled.

In the OI-1, we also identify an interesting correspondence between aquifer pore pressures and column heights. Low shale and sand aquifer pressures are associated with large hydrocarbon columns (fault blocks B and C), whereas fault blocks A and E exhibit relatively high aquifer pressures and short oil columns. Figure 2 provides an explanation for this scenario. In environments of high initial aquifer pressures, the difference between P_p^{crit} and P_p^{ss} is small, the reservoir supports less buoyant hydrocarbon phases, and P_p^{crit} can be reached much more quickly (Figure 2B). Conversely, if initial aquifer pressures are relatively low, the difference between P_p^{crit} and P_p^{ss} is large, the reservoir supports a long hydrocarbon column (i.e., oil and gas), and P_p^{crit} could be reached at a later time (Figure 2A).

The fact that such drastic differences in sand and shale pore pressures can exist in adjacent fault blocks of the same sand (i.e., the OI-1) is very interesting but also quite puzzling. Because water-phase pore pressures in fault blocks B and C are similar, they are hydraulically connected to the same aquifer but decoupled from fault blocks A and E, as inferred from the large pressure contrast (Figures 5C, 8). Because the shale pressures adjacent to the OI-1 reservoirs show similar contrasts, the same mechanisms operating in the sands probably also affected the shales. We believe, therefore, that during burial and structural evolution of the OI-1 sand, a very effective compartmentalization process allowed hydraulic decoupling of the aquifer in these fault blocks and substantial different aquifer pore pressure regimes to develop. Pressure compartmentalization in sedimentary basins as observed in the OI-1 sand has been described with numerous case studies by Powley (1990) and Hunt (1990).

Both effective stress ratios, K and C_{dyn}, are quite variable on top of the OI-1 (Table 6; Figure 5E, F). These variations are the result of variations in both shale and reservoir pore pressures rather than differential stresses (i.e., $S_v - S_{hmin}^{sh}$), which are quite constant throughout the OI-1. K ranges from 0.78 to 0.86. The variations in C_{dyn} range from 0.51 to 0.74. The C_{dyn} values in fault blocks A and E are close to the lower C_{dyn}^{crit} bound (0.55) for $\mu = 0.3$ (Table 6) and also indicate the proximity to dynamic failure of the corresponding hydrocarbon columns. In fault blocks B and C, C_{dyn} is quite high (0.61 and 0.74), supporting the observation that the corresponding hydrocarbon columns are not close to dynamic failure.

The JD Sand

The JD sand is the youngest and shallowest sand considered in this study (Figure 3B). It constitutes the top level of a fourth-order depositional cycle (i.e., top level) of four separate sands (MG through JD) (Figure 3B) that were deposited in a proximal deltaic environment (Alexander and Flemings, 1995). The JD is structurally less complex than the deeper OI-1 or Lentic

(Figure 9). The main structural feature is the northwest-southeast–striking basin bounding growth fault system. On the downthrown side (i.e., mini-basin), two more or less east-west–striking antithetic normal faults subdivide the sand into three distinct fault blocks. In this paper, we focus on fault blocks A and B.

In both fault blocks A and B, the JD has relatively large gas columns (271.6 and 292.7 m [891 and 960 ft], respectively) and short oil columns (39.3 and 6.4 m [129 and 21 ft], respectively) (Table 2; Figure 8A, B). Initial reservoir pore pressures indicate soft overpressures (λ_{ss} = 0.66 and 0.61) (Tables 3, 6; Figure 5). At an equivalent depth, water-phase pressures are equal to within 0.83 MPa (120 psi) (Figure 5C). Pore pressures in the shales (P_p^{sh}) adjacent to the JD are generally comparable with the pore pressures in the reservoirs (Table 6; Figure 8A, B). The λ_{sh} values at the top of the JD (obtained by fitting a linear trend through the provided P_p^{sh} data) are slightly lower than in the reservoir just below (λ_{sh} = 0.61 and 0.66 vs. λ_{ss} = 0.68) (Table 6; Figure 8A, B).

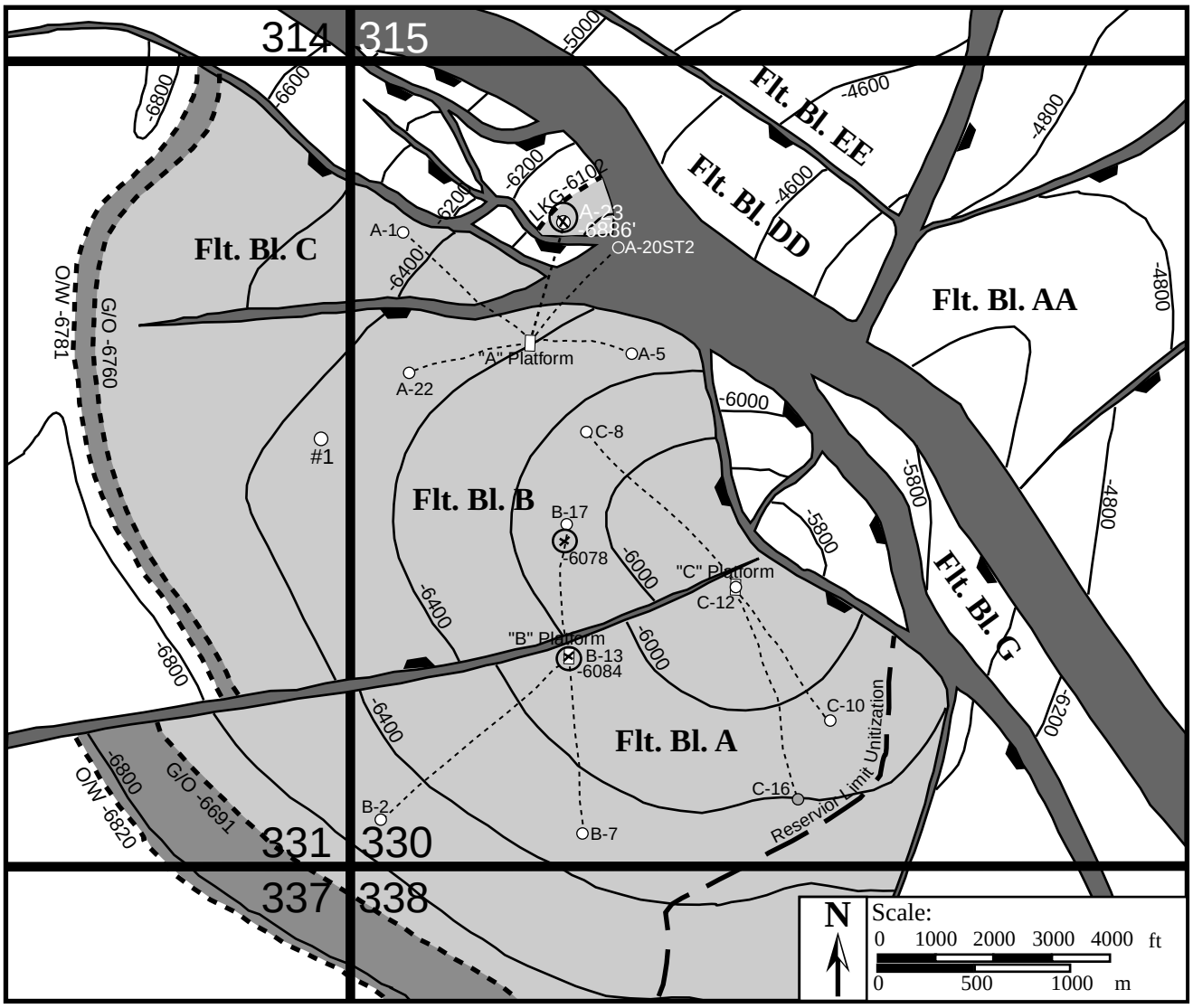

Figure 9. Structure map of the JD reservoir sand for fault block 330 and parts of adjacent fault blocks 331, 337, and 337. Depth contours are in feet SSTVD (conversion: 1 m = 3.28 ft). Well paths are shown as thin dashed lines with points of reservoir penetration (crosses along well paths). Thick dashed lines display interpreted fluid contacts in the individual fault blocks (O/W = oil-water; G/W = gas-water). The depth intervals filled with oil and gas are shown in dark and light gray, respectively. Figure 4 caption describes how this map was generated.

Because no LOTs were run in the shales adjacent to the JD sand, we did not have any direct measurements of least principal stress magnitude available. To obtain S_{hmin}^{sh} values for the shales adjacent to the structural top of the sand reservoirs, we used linear regressions to extrapolate upward from deeper LOTs and FITs (Table 4). In fault block A, we used a LOT carried out near the MG sand (Figure 8A), and in fault block B a FIT conducted near the LF sand (Figure 8B). These tests came from within the same depositional cycle, and their results followed more or less the same trend as those of the LOTs and FITs from the deeper OI-1 sand.

The reservoir pore pressures in the two JD reservoirs are similar, and therefore, the reservoirs are in hydraulic communication across the normal fault separating the fault blocks (Figure 8A, B). Despite the long hydrocarbon columns and the associated large buoyancy effects, pore pressures are significantly lower than the range of critical pore pressures for dynamic capacity (Table 6; Figure 5B).

The effective stress ratios, K and C_{dyn}, are comparable in both fault blocks. In comparison to the deeper levels, K is lower than it is near the OI-1 and Lentic, whereas C_{dyn} is higher. In fault block A, $K = 0.78$ and $C_{dyn} = 0.77$, and in fault block B, $K = 0.79$ and $C_{dyn} = 0.74$ (Table 6; Figure 5E, F). These values reflect the similar pore pressure conditions in both sands and shales and indicate that the hydrocarbon columns in the reservoirs are currently not at failure conditions (Table 7; Figure 8A, B).

Discussion and Implications

The range of critical pore pressures (P_p^{crit}) of a reservoir as defined by the in-situ state of stress represents a state of dynamic equilibrium for which failure and fluid migration would occur (either the reservoir bounding faults slip or the top seals hydraulically fracture). In other words, these critical values define the maximum column heights (i.e., pore pressure) at which a reservoir has reached its dynamic capacity. By applying this dynamic concept to the SEI 330 field, we can infer the specific mechanisms controlling the current hydrocarbon column heights (i.e., pore pressure) and migration in each of the reservoirs previously discussed. We summarize and display all critical information pertaining to the eight reservoirs in Table 6 and Figure 5, respectively.

In the Lentic footwall sand the state of stress is nearly isotropic because of very small differential stresses. As a result, it is difficult to discern between the two dynamic mechanisms, hydraulic fracturing (Figure 1A) or slippage along reservoir bounding faults (Figure 1B), because P_p^{crit} for hydraulic fracturing and P_p^{crit} for fault slip converge. Because reservoir pressures in both Lentic fault blocks A and C are very high and close to or within the range of P_p^{crit}, both mechanisms can be invoked to explain the observed column heights. Thus, the Lentic reservoir appears to have reached its dynamic capacity, the oil columns are at maximum height, and a dynamic fluid flow mechanism appears to be operating, but it is not clear which. Any further increase in pore pressure would cause either the reservoir bounding fault to slip or hydraulic fracturing to occur, resulting in release of the excess pressure. The hatched segments along the faults in Figure 4 are the areas along which we could envision potential fault slip and hydrocarbon migration. Based on the observation of stress-induced borehole breakouts near the Lentic level, Finkbeiner and Zoback (1997, unpublished results) have identified these same faults as potentially active structures controlling the local stress field. Furthermore, we observe small oil columns. Following our discussion for Figure 2, initial water-phase pressures (i.e., before the sand started filling with oil and gas) in the two reservoirs were quite high, allowing only limited volumes of hydrocarbons to accumulate before critical pore pressures are reached and failure occurs. We illustrate this idea in Figure 5C, where the difference between the water- (gray) and hydrocarbon- (black) phase pore pressures indicates the pressure induced by the buoyant hydrocarbon columns. This difference is small in the case of the Lentic sand.

The OI-1 sand within the minibasin shows two interesting things: (1) fault blocks A and E (Figures 5; 8A, D) exhibit relatively high pressures at their tops and short oil columns. Pore pressures are either well within or just at the limit of dynamic equilibrium, which indicates that the two reservoirs are at their dynamic capacity (i.e., the oil columns have reached their maximum height) as controlled by the ambient state of stress. Thus, dynamic mechanisms for hydrocarbon migration and accumulation are operating today in this part of the reservoir. The hatched segments along the faults in Figure 7 are the areas along which we could envision potential fault slip and hydrocarbon migration. Similar to the Lentic level, Finkbeiner and Zoback (1997, unpublished results) have identified these same faults as potentially active structures controlling the local stress field based on the observation of stress-induced borehole breakouts. Again, initial aquifer pore

pressure conditions were quite high in the past, allowing only relatively small amounts of oil to accumulate, thus, limiting the oil column height at present (Figures 2B, 5C). (2) In fault blocks B and C, the columns are much longer and pore pressures are (just) below dynamic equilibrium. Pore pressure data suggest that fault block B is in hydraulic communication with C (Figure 5C). We believe the columns in fault blocks B and C are static and controlled by the presence of a spill point (i.e., leakage below dynamic capacity). In fact, this spill point exists downdip and to the west in fault block C and is approximately equivalent to the mapped oil-water contact, implying that hydrocarbons can migrate westward into the 331 structure (Figure 7) (Rowan et al., 1998). The long oil and gas columns in these two fault blocks (B and C) reflect relatively low initial pore pressures in the past, allowing for large oil and gas columns to develop (Figures 2A, 5C).

In the JD sand, the hydrocarbons are not in dynamic equilibrium. That is, the pore pressures at the top of the JD reservoir are not sufficiently high to either hydrofrac the top seal or induce slip on the bounding faults—even for low coefficients of friction (Figures 5; 8A, B). Thus, neither dynamic mechanism can be invoked that would limit the observed column heights in this sand, and we consider them as being static. In other words, viewed dynamically, the JD reservoirs have not reached their dynamic capacities, and there could be more oil and gas stored in each of these sands than has been observed. Rowan et al. (1998) showed that the JD sand also has a spill point, which is located to the south and west out of the structure, allowing fluids to migrate westward into SEI Block 331. Because fault blocks A and B are hydraulically connected, the column height in fault block A is limited by the same spill point. Initial pore pressures in the JD sand were relatively low, allowing long hydrocarbon columns to develop (Figures 2A, 5C).

Our preferred interpretation for the Lentic sand and two OI-1 reservoirs is that their hydrocarbon columns are dynamically constrained today. In the Lentic horizon, pressures and stresses are so close that we cannot differentiate whether flow is controlled by frictional failure or hydrofracture. At the OI-1 level, in contrast, reservoir blocks A and E clearly have not reached hydrofracture conditions but are within a window where frictional failure along the bounding growth fault may be occurring. We do, however, recognize that a second interpretation is plausible. Namely, the OI-1 reservoirs are not dynamically constrained by the present-day stress field because pore pressures are below the hydrofracture condition today. It is possible that leaking by cross-fault flow is occurring today or occurred as the system evolved (Alexander and Handschy, 1998). Also, the system may have once been at fracture limit, and subsequently pressures dissipated.

Another possibility is that reservoirs having subcritical pore pressures (and long hydrocarbon columns) might have been filled to dynamic capacity (i.e., critical pressures) in the past and then either bled off at a later stage or, when the stresses increased with burial, no further filling (i.e., pressure increase) occurred. As a consequence, pore pressures were driven away from their critical values and are below failure today. Although there is no direct evidence to test these ideas for the SEI 330 field, especially the latter point is interesting because for the past 1 m.y. the SEI 330 minibasin is believed to have been relatively inactive (the subbasin salt has entirely withdrawn, and only small amounts of sediment are currently being deposited). As a result, only small amounts of deformation have occurred at very shallow levels (i.e., in the hydrostatically pressured zone above the reservoirs we studied) accommodating sediment compaction and compaction-driven fluid flow (Alexander and Flemings, 1995). At greater depth (i.e., below the JD level), however, deformation has essentially stalled along the basin bounding growth faults, which favors the concept of faults currently acting as seals rather than conduits and therefore inhibiting fluid flow and reservoir filling. Obviously, this idea does not work for the Lentic sand, which is close to dynamic capacity because the least principal effective stress is almost zero.

Based on the dynamic capacity model and the observed hydrocarbon column heights and pressures, the cross sections in Figures 10 and 11 (see transects in Figure 3) summarize our view of current hydrocarbon migration in the SEI 330 field. The deep Lentic sand (here shown on the minibasin side in Figure 10) experiences severe overpressures close to the minimum principal stresses of the overlying shales. From these deep levels, hydrocarbons migrate upward into the OI sands by hydraulic fracturing (indicated as "Migration Mech. I" in Figure 10) or along the basin bounding growth fault (indicated as "Migration Mech. II" in Figure 10). Depending on the minibasin fault block, the OI-1 sand above offers two possibilities for fluid flow. (1) In fault blocks A, D, and E (Figure 10) pressures are sufficiently high to cause the reservoir bounding faults to slip and to provide valves and pathways for hydrocarbons to migrate further up (indicated as

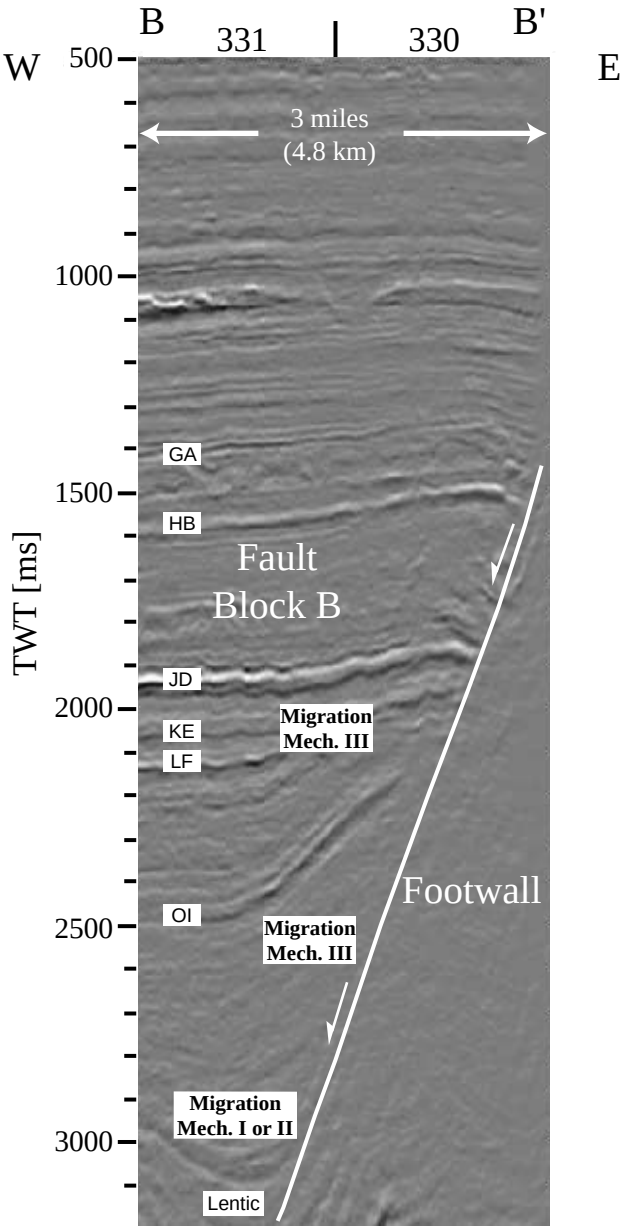

Figure 10. Cross section along transect BB′ (Figure 3A). This cross section was generated from three-dimensional seismic surveys. Positive high amplitudes are shown in black, negative high amplitudes are white. Various reservoir sands are shown within SEI 330 fault block B. The white normal fault displays the main basin bounding growth fault (Figure 3A). "Migration mech. I," "Migration mech. II," and "Migration mech. III" refer to fluid flow by hydraulic fracturing (Figure 1A), active faulting (Figure 1B), and spill point or leakage (Figure 1C), respectively. TWT is two-way traveltime.

"Migration Mech. II" in Figure 10). (2) In fault blocks B and C (Figures 10, 11), however, the reservoir pore pressures are below dynamic equilibrium and column heights appear to be spill-point controlled (indicated as "Migration Mech. III" in Figures 10, 11). All shallower sands (i.e., the JD cycle and above) (Figures 10, 11) exhibit pore pressures far from dynamic equilibrium. We believe that fluids either simply leak out of these sands, driven by their own buoyancy, or the sands communicate hydraulically across faults because of small offsets along these structures (indicated as "Migration Mech. III" in Figures 10, 11).

CONCLUSIONS

We introduced the dynamic capacity model to describe two dynamic mechanisms defined by the in-situ stress state that may control hydrocarbon migration and reservoir column heights by enhancing fracture permeability. We applied this conceptual model to eight sand reservoirs from three depositional cycles (Lentic, OI-1, and JD) in the SEI 330 field. Analysis of pore pressure and stress data from vertical and deviated wells into these reservoirs shows highly variable pore pressures and least principal stresses. Hydrocarbon column heights appear to be controlled by different mechanisms in different parts of the reservoir, suggesting varying mechanisms for fluid flow. In the deepest, severely overpressured Lentic sand, pore pressures are close to the least principal stress, indicating that either natural hydraulic fracturing or fluid flow along active faults may occur. The moderately overpressured OI-1 sand indicates two interesting points. (1) The oil columns in fault blocks A and E are short and exhibit high pressures close to the values expected for dynamic fault slip. Thus, the OI-1 sand in these two reservoir compartments is at dynamic capacity today, and column heights and fluid migration are controlled by active faulting along the main reservoir bounding growth faults. (2) Although the OI-1 reservoirs in fault blocks B and C exhibit very long hydrocarbon columns, pressures are below dynamic equilibrium. Good evidence exists that this sand is spill-point controlled and hydrocarbons can escape into the westward structure of the OI-1. Pore pressures in the shallow and slightly overpressured JD sand are well below critical values for dynamic failure and associated fluid flow. We suggest that either the sands are in a state of being filled, or the hydrocarbon accumulation is controlled by spill points or leaky seals, or the reservoirs were at dynamic capacity in the past and subsequent stalling of basin activity drove pore pressures away from the critical, dynamic value.

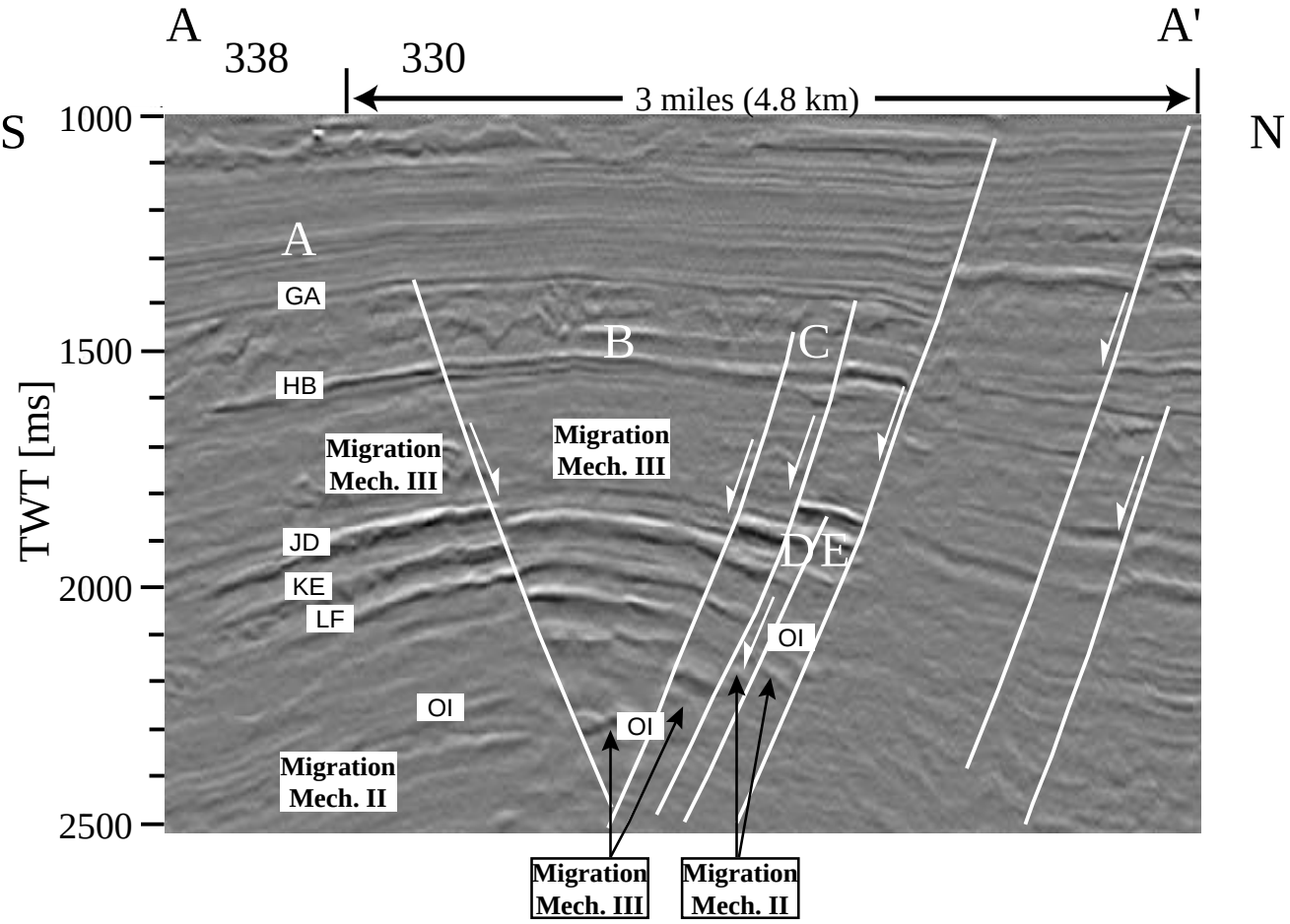

Figure 11. Cross section along transect AA′ showing fault blocks A through E of the minibasin side (Figure 3A). Refer to Figure 10 caption for more detail.

APPENDIX: NOMENCLATURE

Parameter	Description	Units
β	Matrix compressibility	MPa^{-1} (psi^{-1})
C_{dyn}	Dynamic capacity stress ratio	Unitless
C_{dyn}^{crit}	Dynamic capacity stress ratio at critical pore pressure (P_p^{crit})	Unitless
Δt_{ma}	Matrix traveltime	µs/m (µs/ft)
Δt	Wireline traveltime	µs/m (µs/ft)
FIT	Formation integrity test	n/a
φ	Wireline-derived porosity	Unitless
φ_0	Reference porosity	Unitless
K	Shale effective stress ratio	Unitless
λ_{sh}	Normalized shale pressure (P_p^{sh}/S_v)	Unitless
λ_{ss}	Normalized reservoir pressure (P_p^{ss}/S_v)	Untiless
LOT	Leak-off test	n/a
Migration Mech. I	Fluid migration by hydraulic fracturing (Figure 1A)	n/a
Migration Mech. II	Fluid migration by frictional failure along active faults (Figure 1B)	n/a
Migration Mech. III	Fluid migration by leakage or spill point (Figure 1C)	n/a
P_p^{crit}	Critical hydrocarbon-phase reservoir pore pressure	MPa (psi)
P_p^{sh}	Shale pore pressure	MPa (psi)
P_p^{sh} gradient	Shale pore pressure gradient from linear regression	MPa/km (psi/ft)

P_p^{ss}	Hydrocarbon-phase pore pressure in the reservoir	MPa (psi)
S_{hmin}^{sh}	Minimum principal horizontal stress in shale	MPa (psi)
σ_{hmin}^{sh}	Minimum principal horizontal effective stress in shale	MPa (psi)
S_{hmin}^{sh} gradient	Shale minimum principal stress gradient from linear regression	MPa/km (psi/ft)
S_{hmin}^{sh}/S_v	Normalized minimum principal stress in shale	Unitless
S_{Hmax}	Maximum principal horizontal stress	MPa (psi)
SSTVD	Subsea true vertical depth	m (ft)
S_v	Overburden (vertical principal stress)	MPa (psi)
σ_v	Effective overburden (vertical principal effective stress)	MPa (psi)

REFERENCES CITED

Alexander, L. L., and P. B. Flemings, 1995, Geologic evolution of a Plio-Pleistocene salt withdrawal minibasin: Eugene Island Block 330, offshore Louisiana: AAPG Bulletin, v. 79, p. 1737–1756.

Alexander, L. L., and J. W. Handschy, 1998, Fluid flow in a faulted reservoir system: fault trap analysis for the Block 330 field in Eugene Island, south addition, offshore Louisiana: AAPG Bulletin, v. 82, p. 387–411.

Althaus, V. E., 1977, A new model for fracture gradient: Journal of Canadian Petroleum Technology, v. 16, April–June, p. 98–108.

Antonellini, M., and A. Aydin, 1994, Effect of faulting on fluid flow in porous sandstones: AAPG Bulletin, v. 78, p. 355–377.

Barton, C. A., M. D. Zoback, and D. Moos, 1995, Fluid flow along potentially active faults in crystalline rock: Geology, v. 23, p. 683–686.

Batzle, M., and Z. Wang, 1992, Seismic properties of pore fluids: Geophysics, v. 57, p. 1396–1408.

Brudy, M., M. D. Zoback, K. Fuchs, F. Rummel, J. Baumgaertner, 1997, Estimation of the complete stress tensor to 8 km depth in the KTB scientific drill holes: implications for crustal strength: Journal of Geophysical Research, v. 102, p. 18452–18475.

Burrus, J., 1998, Overpressure models for clastic rocks, their relation to hydrocarbon expulsion: a critical reevaluation, *in* B. E. Law, G. F. Ulimshek, and V. I. Slavin, eds., Abnormal pressures in hydrocarbon environments: AAPG Memoir 70, p. 35–63.

Chang, C. T., and M. D. Zoback, 1998, The role of viscous rheology in the state of stress of unconsolidated sands: Society of Petroleum Engineers, Annual Technical Conference and Exhibition, paper 47401, 9 p.

Dickinson, G., 1953, Geological aspects of abnormal reservoir pressures in Gulf Coast Louisiana: AAPG Bulletin, v. 37, p. 410–432.

Engelder, T., and M. P. Fischer, 1994, Influence of poroelastic behavior on the magnitude of minimum horizontal stress, Sh, in overpressured parts of sedimentary basins: Geology, v. 22, p. 949–952.

Engelder, T., and J. T. Leftwich, 1997, A pore pressure limit in overpressured south Texas oil and gas fields, *in* R. C. Surdam, ed., Seals, traps, and the petroleum system: AAPG Memoir 67, p. 255–267.

England, W. A., A. S. MacKenzie, D. M. Mann, and T. M. Quigley, 1987, The movement and entrapment of petroleum fluids in the subsurface: Journal of the Geological Society, v. 144, p. 327–347.

Flemings, P. B., M. D. Zoback, B. A. Bishop, and R. N. Anderson, 1995, State of stress in the Pathfinder well, *in* R. N. Anderson, L. B. Billeaud, P. B. Flemings, S. Losh, J. Whelan, and the GBRN team, eds., Results of the Pathfinder drilling program into a major growth fault: Global Basin Research Network Data Volume, p. 548–615.

Gaarenstroom, L., R. A. J. Tromp, M. C. de Jong, and A. M. Brandenburg, 1993, Overpressures in the central North Sea: implications for trap integrity and drilling safety, *in* J. R. Parker, ed., Petroleum geology of northwest Europe: proceedings of the 4th conference: Geological Society of London, p. 1305–1313.

Gordon, D. S., and P. B. Flemings, 1998, Generation of overpressure and compaction-driven fluid flow in a Plio-Pleistocene growth-faulted basin, Eugene Island 330, offshore Louisiana: Basin Research, v. 10, p. 177–196.

Grauls, D. J., and J. M. Baleix, 1994, Role of overpressures and in-situ stresses in fault-controlled hydrocarbon migration: a case study: Marine and Petroleum Geology, v. 11, p. 734–742.

Hart, B. S., P. B. Flemings, and A. Deshpande, 1995, Porosity and pressure: role of compaction disequilibrium in the development of geopressures in a Gulf Coast Pleistocene basin: Geology, v. 23, p. 45–48.

Heppard, P. D., H. S. Cander, and E. B. Eggertson, 1998, Abnormal pressure and the occurrence of hydrocarbons off the east coast of Trinidad, West Indies, *in* B. E. Law, G. F. Ulimshek, V. I. Slavin, eds., Abnormal pressures in hydrocarbon environments: AAPG Memoir 70, p. 215–246.

Hickman, S., R. Sibson, and R. Bruhn, 1995, Introduction to special section: mechanical involvement of fluids in faulting: Journal of Geophysical Research, v. 100, p. 12831–12840.

Holland, D. S., J. B. Leedy, and D. R. Lammlein, 1990, Eugene Island Block 330 field—USA, offshore Louisiana, *in* E. A. Beaumont and N. H. Foster, eds., Structural traps III, tectonic fold and fault traps: AAPG Treatise of Petroleum Geology Atlas of Oil and Gas Fields, p. 103–143.

Hooper, E. C. D., 1991, Fluid migration along growth faults in compacting sediments: Journal of Petroleum Geology, v. 14. no. 2, p. 161–180.

Hubbert, M. K., and D. G. Willis, 1957, Mechanics of hydraulic fracturing: Transactions of the American Institute of Mining and Engineering, v. 210, p. 115–205.

Hunt, J. M., 1990, Generation and migration of petroleum from abnormally pressured fluid compartments: AAPG Bulletin, v. 74, p. 1–12.

Ingram, G. M., and J. L. Urai, 1997, Top seal leakage through faults and fractures: the role of mudrock properties: Proceedings of the Geological Society Conference on Mudrocks at the Basin Scale: Properties, Controls, and Behaviour, 26 p.

Jaeger, J. C., and N. G. W. Cook, 1979, Fundamentals of rock mechanics, 3d ed.: New York, Chapman and Hall, 513 p.

Leach, W. G., 1993a, New exploration enhancements in S Louisiana Tertiary sediments: Oil & Gas Journal, v. 91, no. 9, p. 83–87.

Leach, W. G., 1993b, Fluid migration, HC concentration in south Louisiana Tertiary sands: Oil & Gas Journal, v. 91, no. 11, p. 71–74.

Leach, W. G., 1993c, Maximum hydrocarbon window determination in south Louisiana: Oil & Gas Journal, v. 91, no. 13, p. 81–84.

Makurat, A. N., 1985, The effect of shear displacement on the per-

meability of natural rough joints, *in* S. P. Neuman, ed., Hydrogeology of rocks of low permeability: International Association of Hydrogeologists Memoir 17, p. 99–106.

Mello, U. T., and G. D. Karner, 1996, Development of sediment overpressure and its effect to thermal maturation: application to the Gulf of Mexico basin: AAPG Bulletin, v. 80, p. 1367–1396.

Nehring, R., 1991, Oil and gas resources, *in* A. Salvador, ed., The Gulf of Mexico Basin: decade of North American geology: Geological Society of America, v. J, p. 445–494.

Nur, A. M., and J. Walder, 1990, Time-dependent hydraulics of the Earth's crust, *in* Geophysics Study Committee, National Research Council, eds., The role of fluids in crustal processes: Washington, D.C., National Academy Press, p. 113–127.

Ostermeier, R. M., 1993, Deepwater Gulf of Mexico turbidites: compaction effects on porosity and permeability: Society of Petroleum Engineers Formation Evaluation, v. 10, no. 2, p. 79–85.

Pilkington, P. E., 1978, Fracture gradient estimates in Tertiary basins: Petroleum Engineer International, v. 8, no. 5, p. 138–148.

Powley, D. E., 1990, Pressures and hydrogeology in petroleum basins: Earth-Science Reviews, v. 29, p. 215–226.

Rowan, M. G., B. S. Hart, S. Nelson, P. B. Flemings, and B. D. Trudgill, 1998, Three-dimensional geometry and evolution of a salt-related growth-fault array: Eugene Island 330 field, offshore Louisiana, Gulf of Mexico: Marine Petroleum Geology, v. 15, p. 309–328.

Rubey, W. W., and M. K. Hubbert, 1959, Overthrust belt in geosynclinal area of western Wyoming in light of fluid pressure hypothesis, 2: role of fluid pressure in mechanics of overthrust faulting: Geological Society of America Bulletin, v. 70, p. 167–205.

Segall P., and S. D. Fitzgerald, 1996, A note on induced stress changes in hydrocarbon and geothermal reservoirs: Tectonophysics, v. 289. p. 117–128.

Segall P., J. R. Grasso, and A. Mossop, 1994, Poroelastic stressing and induced seismicity near the Lacq gas field, southwestern France: Journal of Geophysical Research, v. 90, p. 15423–15438.

Sibson, R. H., 1992, Implications of fault-valve behavior for rupture nucleation and recurrence: Tectonophysics, v. 211, p. 283–293.

Smith, D. A., 1966, Theoretical considerations of sealing and non-sealing faults: AAPG Bulletin, v. 50, p. 363–374.

Stump, B. B., P. B. Flemings, T. Finkbeiner, and M. D. Zoback, 1998, Pressure differences between overpressured sands and bounding shales of the Eugene Island 330 field (offshore Louisiana, USA) with implications for fluid flow induced by sediment loading, *in* A. Mitchell and D. Grauls, eds., Overpressures in petroleum exploration: workshop proceedings: Elf Exploration Production Memoir 22, p. 83–92.

Terzaghi, K., 1943, Theoretical soil mechanics: New York, John Wiley and Sons, 796 p.

Traugott, M. O., 1997, Pore/fracture pressure determinations in deep water: Deepwater Technology, v. 4, no. 8, p. 68–70.

Traugott, M. O., and P. D. Heppard, 1994, Prediction of pore pressure before and after drilling—taking the risk out of drilling overpressured prospects: AAPG Hedberg Research Conference, v. 70, p. 215–246.

Wang, C. Y., N. Mao, and F. T. Wu, 1979, The mechanical property of montmorillonite clay at high pressure and implication on fault behavior: Geophysical Research Letters, v. 6, p. 476–478.

Wang, C. Y., N. Mao, and F. T. Wu, 1980, Mechanical properties of clays at high pressures: Journal of Geophysical Research, v. 85, p. 1462–1468.

Watts, N. L., 1987, Theoretical aspects of cap-rock and fault seals for single- and two-phase hydrocarbon columns: Marine and Petroleum Geology, v. 4, p. 274–307.

Zoback, M. D, and J. H. Healy, 1984, Friction, faulting, and in-situ stress: Annales Geophysicae, v. 2, p. 689–698.

Zoback, M. D, and J. H. Healy, 1992, In-situ stress measurements to 3.5 km depth in the Cajon Pass scientific borehole: implications for the mechanics of crustal faulting: Journal of Geophysical Research, v. 97, p. 5039–5057.